A Strategy to Trap Oxygen and to Kill Cancer Cells by Photodynamic Therapy.

Marie Gaschard,[a] Daniel L. Stares,[b] Manuel A. Gallardo-Villagrán,[ac] David Yannick Leger,[c] Bertrand Liagre,[c] Christoph A. Schalley[b] and Bruno Therrien[a*]

[a] Institute of Chemistry, University of Neuchâtel, Avenue de Bellevaux 51, 2000 Neuchâtel, Switzerland.

[b] Institute of Chemistry and Biochemistry of Freie Universität Berlin, Arnimallee 20, 14195 Berlin, Germany.

[c] Département de Biochimie et Biologie Moléculaire, Laboratoire PEIRENE, Faculté de Pharmacie, 2 rue du Docteur Marcland, 87025 Limoges, France.

*corresponding author: bruno.therrien@unine.ch

Keywords

Arene Ruthenium; Anthracene; Singlet Oxygen; Photodynamic Therapy; Phototoxicity; Prostatic Cancer Cells.

Abstract

Low oxygen concentration in solid cancer tumors leads to resistance, especially when dealing with photodynamic therapy (PDT) treatments. In fact, the presence of oxygen is mandatory to obtain an efficient PDT treatment. The synthesis of new oxygen carriers, specifically targeting cancer cells, appears to be an elegant strategy to tackle this issue. With this in mind, we have synthetized 15 arene ruthenium(II) assemblies containing different anthracenyl-based ligands in which the anthracenyl moieties were used to capture O_2. We present their synthesis and characterization, as well as their photo-oxygenation and their toxicity/phototoxicity behavior on DU145 prostatic cancer cells. The possibility to transport oxygen via the formation of endoperoxides was further confirmed by mass spectrometry.

1. Introduction

The burden of cancers on our societies represents one of the biggest challenges of the 21st century [1, 2]. Its human and economic costs force us to continuously find new solutions to better fight the disease. With this in mind, it is important to understand what a cancer cell is and what its mechanisms are to understand its dangers to our body. In tunmors, cancerous cells are often under hypoxic conditions [3], especially those located far from blood vessels (100-150 µm), where the oxygen concentration is low [3-5]. Cancer cells need oxygen to function, but unlike healthy cells, they are able to develop mechanisms to survive under hostile conditions [6,7]. The adaptation to oxygen levels involves a major transcriptional response, the Hypoxia-Inducible Factor (HIF) pathway, that can be seen as a cellular oxygen sensor (Fig. 1) [8-10]. This pathway is working in both normoxia (normal oxygen concentration) and hypoxia situations. When hypoxia appears in cancer cells, the HIF-pathway provokes the activation of adaptative mechanisms, with biological consequences such as morphological and metabolic modifications, or the development of new blood vessels and metastases, thus allowing tumor cells to escape from death. In addition, all these changes cause a degree of anti-cancer treatment resistance (Fig. 1) [9, 10]. So, there is a real necessity to develop new therapies that can disrupt these adaptive mechanisms and to ensure cancer cell death [3,9,11].

One of them is PhotoDynamic Therapy (PDT) [12-14]. It can be viewed as a promising treatment since its high selectivity and efficiency come from the combination of three elements (light, photosensitizer and oxygen), in the same spatio-temporal settings (Fig. 2) [15,16]. In fact, after the irradiation of a photosensitizer (a molecule able to capture light energy, PS), the energy can be transferred to either oxygen or to a smaller extent to a biological substrate that can promote the formation of Reactive Oxygen Species

(ROS). The redox balance can then be surpassed, thus leading to an oxidative stress, provoking cell death [17,18].

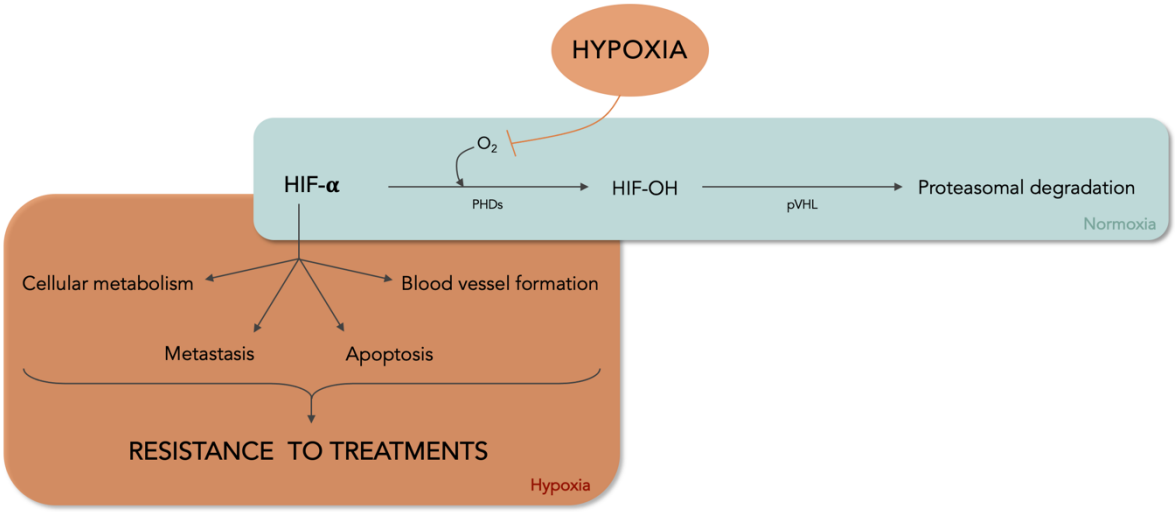

Fig. 1. Simplified mechanism of HIF-α during normoxia and hypoxia. During normoxia, HIF-α is hydrolyzed, before being degraded by a proteasome. During hypoxia, HIF-α is not degraded and its accumulation within the cell provokes the modification of common physiological events, which lead to the survival of cancer cells (PHDs: prolyl-4-hydroxylases; pVHL: Von Hippel Lindau protein) [10, 12].

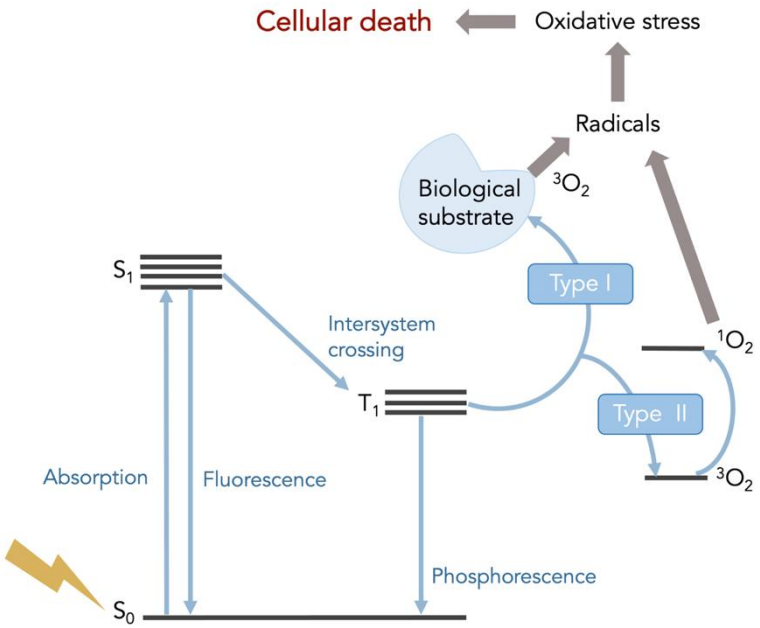

Fig. 2. Modified Jablonski diagram: energy transfers between light, PS and O_2 during PDT.

Understanding the hypoxic environment of cancer cells, such treatment can suffer from a lack of oxygen, and can be inefficient despite its great potential. One of the solutions

is to deliver the missing oxygen into the cancerous area, by controlling the singlet oxygen formation through the design of PS and/or delivery system [19]. With this purpose in mind, it can be interesting to build new molecular structures that can carry oxygen together with the PS in the treated area in order to maximize the PDT effect with a higher singlet oxygen production.

The literature shows the possibility to use supramolecular assemblies with transition metals for PDT purposes [20]. Our team has demonstrated the great ability of arene ruthenium(II) complexes to trap and transport a photosensitizer to cancer cells [21]. Moreover, we have established that the PS is phototoxic for cells only when it is released from the hydrophobic cavity of the assembly, where it was shielded [21]. Therefore, the idea is to adapt this general structure, consisting of arene ruthenium(II) cages with oxygen carrier patterns and determine if they could have a potential use for PDT and for the transport of molecular oxygen.

In this study, anthracene derivatives were chosen, among several other candidates, to play the role of oxygen carriers [22-24]. Anthracene belongs to the acene class and correspond to the most intensively studied oxygen carriers [23,24]. Since the discovery of the “labile bonding of oxygen to carbon” in 1926 by Dufraisse and Moureu, researchers have elucidated the mechanism of the [4+2] cycloaddition of oxygen on the anthracene core (similar to a normal Diels-Alder reaction) [25-29]. Moreover, the potential of using functionalized anthracenyl derivatives coordinated to metal-based PDT agents was recently acknowledged [29]. Indeed, recent studies about metal-based anthracene derivatives were published by Fudickar and Linker [24, 30].

Herein, the synthesis of 15 new arene ruthenium(II) complexes incorporating anthracenyl moieties ($\mathbf{A}_{\mathbf{anthr}}$) are presented. The structure of the metalla-assemblies was adapted to link several pyridyl-anthracenyl ligands. The ability to capture oxygen

was evaluated in the presence of an external photosensitizer. In addition, their cytotoxicity and phototoxicity on DU145 prostatic cancer cells were determined.

2. Experimental section

2.1. Materials

All commercially available chemicals and solvents were purchased and used as received without further purification. All solvents were dried before use on silica, molecular sieve or by distillation. All reactions were performed under an inert N_2 atmosphere (unless specified otherwise). Thin layer chromatography (TLC) plates were purchased from Merck. Purifications by column chromatography were realized on silica gel 60 Å (32-63 Mesh) and technical solvents were used for elution. Removal of solvents was performed on a rotary evaporator at 40 °C and under reduced pressure. Final products were dried under high vacuum (around 10^{-3} mbar) at room temperature.

2.2. Instrumentation and Methods

NMR spectra were recorded on a Bruker Avance II 400 Spectrometer (Karlsruhe, Germany), using deuterated solvents as internal standard. The chemical shifts are referenced to deuterated solvent residual peaks ($CDCl_3$: δ = 7.26 ppm; CD_2Cl_2: δ = 5.32 ppm; $(CD_3)_2CO$: δ = 2.05 ppm; and CD_3CN: δ = 1.94 ppm). UV−Visible absorption spectra were recorded with a PerkinElmer Lambda 25 spectrophotometer (Waltham, Massachusetts, USA) using quartz cells having an optical path length of 1 cm. IR spectra were recorded with a Thermoscientific Nicolet iS5 spectrometer (Waltham, Massachusetts, USA). Electrospray ionization mass spectrometry (ESI-MS) spectra were obtained in a positive mode with a LCQ Finnigan mass spectrometer (San Jose, California, USA) at the University of Fribourg (Switzerland). Ruthenium(II) assemblies were studied by mass spectroscopy at Freie Universität Berlin (Germany). ESI-MS were recorded with a Synapt G2-S HDMS Q-TOF travelling wave ion mobility mass spectrometer (Waters Co., Milford, Massachusetts, USA). Microanalyses were carried

out by the Mikroelementaranalytisches Laboratorium, ETH Zürich (Zürich, Switzerland). Irradiation studies with O_2 were performed using a Luzchem LZC-ORG photometer (Montreal, QC, Canada) equipped with the corresponding lamp (cool white lamp, Hg, 8 W, Sylvania® F8T5/CW).

2.3. Synthesis and Characterization

Precursors molecules were prepared according to published methods: $[Ru_2(\eta^6\text{-}p\text{-cymene})_2(\mu_4\text{-oxa})Cl_2]$ [31], $[Ru^2(\eta^6\text{-}p\text{-cymene})^2(\mu^4\text{-dobq})Cl_2]$ [32], $[Ru_2(\eta^6\text{-}p\text{-cymene})_2(\mu_4\text{-donq})Cl_2]$ [33], $[Ru(\eta^6\text{-}p\text{-cymene})(pta)Cl_2]$ [34], $[\{(\eta^6\text{-}p\text{-cymene})Ru(\mu_2\text{-Cl})Cl\}_2]$ [35], 9,10-bis(4-pyridyl)anthracene [36], 9,10-bis(3-pyridyl)anthracene [36], 9,10-bis((pyridin-4-yl)vinyl)anthracene [37, 38], 9,10-bis(3,3'-ethynylpyridyl) anthracene [39], 9-(4-pyridyl)anthracene [36], 9-(3-pyridyl)anthracene [36] and 9-((pyridin-4-yl)vinyl)anthracene [37, 38]. Synthetic details for $\mathbf{L_{anthr}}$ are provided in the supporting information.

*2.3.1. General procedure for the synthesis of ruthenium rectangles with anthracenyl derivatives (**A_1** – **A_9**).*

A mixture of metalla-clip (**Ru-oxa**, **Ru-dobq**, or **Ru-donq**, 0.27 mmol) and silver trifluoromethanesulfonate (139 mg, 0.54 mmol) was dissolved in CH_2Cl_2 and stirred for 3 h at room temperature. The mixture was filtrated in order to eliminate silver chloride. The resulting solution was added to a CH_2Cl_2 solution containing the anthracene ligand ($\mathbf{L_1}$-$\mathbf{L_4}$, 0.27 mmol). Then, the mixture was refluxed overnight and consequently concentrated under vacuum. The concentrated solution was slowly poured into cold Et_2O to induce precipitation. After filtration, the metalla-rectangles were dried under vacuum.

$[Ru_4(\eta^6\text{-}p\text{-cymene})_4(\mu^4\text{-dobq})_2(\mu^2\text{-}L_1)_2][CF_3SO_3]_4$ (A_1): Red solid (374 mg, 56%). ^{1}H-NMR (CD_3CN, 400 MHz): δ 8.46 (d, *J* = 5.6 Hz, 8H), 7.50 (m, 8H), 7.27 (dd, *J* = 6.8 Hz

and *J* = 3.2 Hz, 8H), 6.82 (m, 8H), 6.01 (d, *J* = 6 Hz, 8H), 5.93 (s, 4H), 5.81 (d, *J* = 6.4 Hz, 8H), 2.96 (sept, *J* = 6.8 Hz, 4H), 2.28 (s, 12H), 1.41 (d, *J* = 8.8 Hz, 24H). $^{13}C\{^{1}H\}$-NMR (CD_3CN, 100 MHz): δ 184.55 (8C), 184.6 (8C), 153.1 (8C), 133.1 (12C), 128.9 (8C), 128.3 (4C), 126.3 (8C), 125.5 (8C), 103.6 (4C), 101.8 (4C), 98.8 (4C), 83.6 (8C), 82.2 (8C), 31.3 (4C), 21.53 (8C), 17.4 (4C). *D*(CD_3CN): 6.76 x 10^{-10} $m^2 \cdot s^{-1}$. IR (cm^{-1}): 3071 (w; C–H_{ar}), 2969 (w; C–H_{ar}), 1610 (w; C=C_{ar}), 1518 (s; C=C_{ar}), 1374 (s; C=C_{ar}), 1255 (s; C=C_{ar}), 1153 (m; C=C_{ar}), 1028 (s; C=C_{ar}), 635 (s; C–H_{ar}). ESI–MS (+); [M-4(CF_3SO_3)$^-$]$^{4+}$ *exp.* 470.5728 found. 470.5757; UV−vis [1.0 × 10^{-5} M, CH_3CN; λ_{max}, nm (ε, $M^{-1} \cdot m^{-1}$)]: 306 (4.6 × 10^4), 361 (2.5 × 10^4), 379 (2.5 × 10^4), 396 (5.5 × 10^4), 482 (3.3 × 10^4), 513 (3.3 × 10^4).

[Ru_4(η^6-*p*-cymene)$_4$(μ^4-donq)$_2$(μ^2-L_1)$_2$][CF_3SO_3]$_4$ (A_2): Green solid (341 mg, 49%). ^{1}H-NMR (CD_3CN, 400 MHz): δ 8.92 (m, 8H), 7.78 (m, 8H), 7.59 (m, 24H), 6.30 (m, 8H), 5.83 (m, 8H), 2.97 (sept, *J* = 6.5 Hz, 4H), 1.96 (s, 12H), 1.32 (m, 24H). $^{13}C\{^{1}H\}$-NMR (CD_3CN, 100 MHz): δ 156.2 (4C), 156.1 (4C), 152.5 (4C), 139.9 (8C), 130.7 (4C), 129.8 (4C), 129.6 (8C), 127.7 (8C), 127.3 (8C), 126.9 (8C), 123.7 (8C), 120.5 (4C), 111.0 (4C), 88.6 (8C), 86.4 (8C), 31.9 (4C), 22.6 (4C), 22.4 (4C), 18.5 (4C). *D*(CD_3CN): 8.96 x 10^{-10} $m^2 \cdot s^{-1}$. IR (cm^{-1}): 3073 (w; C–H_{ar}), 2973 (w; C–H_{ar}), 1612 (w; C=C_{ar}), 1256 (s; C=C_{ar}), 1167 (m; C=C_{ar}), 1029 (s; C=C_{ar}), 636 (s; C–H_{ar}). UV−vis [1.0 × 10^{-5} M, CH_3CN; λ_{max}, nm (ε, $M^{-1} \cdot m^{-1}$)]: 340 (1.2 × 10^4), 358 (1.8 × 10^4), 379 (2.5 × 10^4), 398 (4.2 × 10^4).

[Ru_4(η^6-*p*-cymene)$_4$(μ^4-oxa)$_2$(μ^2-L_2)$_2$][CF_3SO_3]$_4$ (A_3): Yellow solid (270 mg, 42%). ^{1}H-NMR (CD_3CN, 400 MHz): δ 8.97 (m, 4H),8.67 (m, 4H), 8.06 (m, 4H), 7.84 (m, 4H), 7.56 (m, 16H), 5.67 (m, 16H), 2.84 (m, 4H), 2.11 (s, 6H), 2.07 (s, 6H), 1.30 (m, 24H). $^{13}C\{^{1}H\}$-NMR (CD_3CN, 100 MHz): δ 155.3 (4C), 153.7 (4C), 142.9 (2C), 142.7 (2C), 137.5 (4C), 130.8 (4C), 129.2 (4C), 127.7 (4C), 127.6 (4C), 127.0 (4C), 126.8 (4C),

123.7 (4C), 120.5 (4C), 102.7 (2C), 102.3 (2C), 98.2 (4C), 87.1 (2C), 87.0 (2C), 84.5 (2C), 83.4 (4C), 81.6 (4C), 76.9 (2C), 31.8 (2C), 31.7 (2C), 22.6 (4C), 22.4 (2C), (2C), 22.3 (2C), 18.5 (2C), 18.0 (2C). *D*(CD_3CN): 9.41 x 10^{-10} $m^2 \cdot s^{-1}$. IR (cm^{-1}): 3068 (w; C–H_{ar}), 2974 (w; C–H_{ar}), 1672 (m; C=C_{ar}), 1627 (s; C=C_{ar}), 1274 (s; C=C_{ar}), 1254 (s; C=C_{ar}), 1157 (m; C=C_{ar}), 1028 (s; C=C_{ar}), 636 (s; C–H_{ar}). UV−vis [1.0 × 10^{-5} M, CH_3CN; λ_{max}, nm (ε, M−1·m−1)]: 341 (1.5 × 10^4), 356 (2.3 × 10^4), 377 (3.4 × 10^4), 399 (4.6 × 10^4).

[Ru_4(η^6-*p*-cymene)$_4$(μ^4-dobq)$_2$(μ^2-L_2)$_2$][CF_3SO_3]$_4$ (A_4): Red solid (361 mg, 54%). ^{1}H-NMR (CD_3CN, 400 MHz): δ 8.81 (d, *J* = 4.8 Hz, 4H), 8.66 (s, 4H), 7.93 (d, *J* = 8 Hz, 4H), 7.70 (d, *J* = 6.6 Hz, 4H), 7.63 (m, 8H), 7.46 (m, 12H), 5.82 (m, 16H), 2.84 (sept, *J* = 7 Hz), 1.96 (s, 12H), 1.29 (m, 24H). ^{13}C{^{1}H}-NMR ((CD_3)$_2$CO, 100 MHz): δ 185.3 (8C), 151.6 (2C), 151.2 (2C), 148.6 (2C), 147.6 (2C), 140.8 (8C), 136.6 (4C), 133.8 (8C), 127.7 (2C), 127.6 (2C), 127.2 (2C), 126.9 (2C),126.4 (4C), 120.8 (8C), 111.1 (4C), 105.8 (4C), 105.0 (4C), 84.4 (8C), 83.3 (8C), 32.2 (4C), 22.7 (8C), 18.5 (4C). *D*(CD_3CN): 6.39 x 10^{-10} $m^2 \cdot s^{-1}$. IR (cm^{-1}): 3072 (w; C–H_{ar}), 2968 (w; C–H_{ar}), 1631 (w; C=C_{ar}, 1518 (s; C=C_{ar}), 1374 (s; C=C_{ar}), 1255 (s; C=C_{ar}), 1156 (m; C=C_{ar}), 1027 (s; C=C_{ar}), 635 (s; C–H_{ar}). ESI–MS (+); [M-4(CF_3SO_3)$^-$]$^{4+}$ *exp.* 470.5744 found. 470.5762; UV−vis [1.0 × 10^{-5} M, CH_3CN; λ_{max}, nm (ε, $M^{-1} \cdot m^{-1}$)]: 303 (4.3 × 10^4), 362 (3.2 × 10^4), 381 (4.2 × 10^4), 402 (5.9 × 10^4).

[Ru_4(η^6-*p*-cymene)$_4$(μ^4-donq)$_2$(μ^2-L_2)$_2$][CF_3SO_3]$_4$ (A_5): Green solid (271 mg, 39%). ^{1}H-NMR (CD_3CN, 400 MHz): δ 9.04 (m, 4H), 8.86 (m, 4H), 8.14 (m, 4H),7.85 (m, 4H), 7.37 (m, 24H), 5.81 (m, 16H), 2.85 (sept, *J* = 6.8 Hz, 4H), 2.05 (m, 12H), 1.24 (m, 24H). ^{13}C{^{1}H}-NMR (CD_3CN, 100 MHz): δ 156.8 (2C), 155.9 (2C), 155.3 (2C), 151.1 (2C), 143.3 (2C) 142.9 (2C), 137.2 (8C), 135.8 (4C), 133.3 (2C), 133.0 (2C), 130.9 (4C), 129.3 (4C), 127.7 (4C), 127.5 (4C), 127.0 (2C), 126.8 (2C), 123.7 (8C), 120.5 (4C),

110.9 (4C), 106.6 (4C, C_{CF3SO3}), 102.3 (4C), 87.0 (4C), 86.0 (4C), 84.6 (2C), 84.5 (4C), 84.4 (2C), 31.7 (4C), 22.4 (4C), 22.3 (4C), 18.5 (4C). *D*(CD_3CN): 9.67 x 10^{-10} $m^2 \cdot s^{-1}$. IR (cm^{-1}): 3070 (w; C–H_{ar}), 2975 (w; C–H_{ar}), 1611 (w; C=C_{ar}), 1274 (s; C=C_{ar}), 1258 (s; C=C_{ar}), 1156 (m; C=C_{ar}), 1030 (s; C=C_{ar}), 637 (s; C–H_{ar}). UV−vis [1.0 × 10^{-5} M, CH_3CN; λ_{max}, nm (ε, $M^{-1} \cdot m^{-1}$)]: 341 (1.9 × 10^4), 359 (3.1 × 10^4), 377 (4.5 × 10^4), 398 (5.3 × 10^4).

[Ru_4(η^6-*p*-cymene)$_4$(μ^4-dobq)$_2$(μ^2-L_3)$_2$][CF_3SO_3]$_4$ (A_6): Red solid (502 mg, 72%). ^{1}H-NMR (CD_3CN, 400 MHz): δ 8.18 (d, *J* = 6 Hz, 8H), 8.05 (d, *J* = 16.4 Hz, 4H), 7.90 (dd, *J* = 6.8 Hz and *J* = 3.6 Hz, 8H), 7.66 (d, *J* = 6 Hz, 8H), 7.17 (dd, *J* = 6.8 Hz and *J* = 3.2 Hz, 8H), 6.72 (dd, *J* = 16.4 Hz, 4H), 5.95 (d, *J* = 6 Hz, 8H), 5.78 (s, 4H), 5.73 (d, *J* = 6 Hz, 8H), 2.88 (sept, *J* = 6.8 Hz, 4H), 2.20 (s, 12H), 1.36 (d, *J* = 6.8 Hz, 24H). ^{13}C{^{1}H}-NMR (CD_3CN, 100 MHz): δ 185.0 (8C), 153.8 (8C), 148.5 (4C), 134.6 (4C), 133.8 (4C), 132.1 (4C), 129.5 (8C), 126.8 (8C), 124.1 (8C), 104.6 (4C), 102.4 (4C), 98.8 (4C), 84.6 (8C), 82.7 (8C), 32.16 (4C), 22.5 (8C), 18.4 (4C). *D*(CD_3CN): 6.09 x 10^{-10} $m^2 \cdot s^{-1}$. IR (cm^{-1}): 3072 (w; C–H_{ar}), 2974 (w; C–H_{ar}), 1610 (w; C=C_{ar}), 1521 (s; C=C_{ar}), 13745 (s; C=C_{ar}), 1257 (s; C=C_{ar}), 1158 (m; C=C_{ar}), 1028 (s; C=C_{ar}), 636 (s; C–H_{ar}). ESI–MS (+); [M-4(CF_3SO_3)$^-$]$^{4+}$ *exp.* 496.5901 found. 496.5914; UV−vis [1.0 × 10^{-5} M, CH_3CN; λ_{max}, nm (ε, $M^{-1} \cdot m^{-1}$)]: 399 (5.3 × 10^4), 458 (5.5 × 10^4), 513 (3.8 × 10^4).

[Ru_4(η^6-*p*-cymene)$_4$(μ^4-oxa)$_2$(μ^2-L_4)$_2$][CF_3SO_3]$_4$ (A_7): Yellow solid (494 mg, 74%). ^{1}H-NMR ($(CD_3)_2CO$, 400 MHz): δ 8.64 (m, 8H, H_h and H_k), 8.16 (m, 12H, H_i and H_q), 7.65 (t, *J* = 6.6 Hz, 4H, H_j), 7.34 (m, 8H, H_r), 6.20 (dd, *J* = 11.6 Hz and *J* = 6.0 Hz, 8H, H_d), 6.05 (m, 8H, H_e), 3.04 (sept, *J* = 6.6 Hz, 4H, H_b), 2.35 (s, 12H, H_g), 1.45 (d, *J* = 6.8 Hz, 12H, H_a), 1.43 (d, *J* = 6.8 Hz, 12H, H_a). ^{13}C{^{1}H}-NMR ($(CD_3)_2CO$, 100 MHz): δ 172.1 (2C), 172.0 (2C), 154.7 (4C), 152.5 (4C), 143.8 (4C), 137.2 (4C), 131.4 (4C), 128.2 (8C), 127.7 (4C), 127.2 (8C), 123.78 (4C), 120.9 (4C), 117.9 (4C, C_{CF3SO3}), 103.4 (4C),

99.0 (4C), 97.4 (4C), 92.9 (4C), 83.3 (2C), 83.2 (2C), 83.1 (4C), 82.9 (2C), 82.8 (2C), 82.3 (4C), 32.0 (4C), 22.7 (4C), 22.4 (4C), 18.2 (4C). *D*($(CD_3)_2CO$): 6.67 x 10^{-10} $m^2 \cdot s^{-1}$. IR (cm^{-1}): 3079 (w; C–H_{ar}), 2211 (w; C≡C), 1625 (s; C=O), 1482 (m; C=C_{ar}), 765 (m; C–H_{ar}), 636 (s; C–H_{ar}). UV−vis [1.0 x 10^{-5} M, EtOH; λ_{max}, nm (ε, $M^{-1} \cdot cm^{-1}$)]: 271 (3.1 × 10^5), 312 (7.5 × 10^4), 437 (7.6 × 10^4), 459 (7.8 × 10^4), 742 (7.3 × 10^3). Anal. calc. for $C_{104}H_{88}F_{12}N_4O_{20}Ru_4S_4$ (2474.48): C 50.48, H 3.59, N 2.27; Found: C 50.56, H 3.68, N 2.22.

[Ru_4(η^6-*p*-cymene)$_4$(μ^4-dobq)$_2$(μ^2-L_4)$_2$][CF_3SO_3]$_4$ (A_8): Red solid (472 mg, 68%). ^{1}H-NMR ($(CD_3)_2CO$, 400 MHz): δ 8.64 (d, *J* = 7.6 Hz, 4H), 8.58 (s, 4H), 8.31 (d, *J* = 6.0 Hz, 4H),8.05 (dd, *J* = 6.8 Hz and *J* = 3.2 Hz, 8H), 7.70 (t, *J* = 6.8 Hz, 4H), 7.47 (m, 8H), 6.34 (d, *J* = 6.0 Hz, 8H), 6.11 (d, *J* = 6.0 Hz, 8H), 5.96 (s, 4H), 3.04 (sept, *J* = 6.6 Hz, 4H), 2.33 (s, 12H), 1.42 (d, *J* = 6.8 Hz, 24H). ^{13}C{^{1}H}-NMR ($(CD_3)_2CO$, 100 MHz): δ 184.4 (8C), 155.3 (4C), 153.2 (4C), 142.8 (4C), 131.3 (8C), 128.3 (8C), 127.3 (4C), 127.1 (8C), 124.0 (1C), 123.3 (1C), 120.8 (4C), 117.7 (2C), 104.8 (4C), 102.4 (4C), 100.1 (4C, C_{CF3SO3}), 97.0 (4C), 92.1 (4C), 90.6 (4C), 84.6 (8C), 82.6 (8C), 32.1 (4C), 22.5 (8C), 18.24 (4C). *D*($(CD_3)_2CO$): 6.04 x 10^{-10} $m^2 \cdot s^{-1}$. IR (cm^{-1}): 3075 (w; C–H_{ar}), 2198 (w; C≡C), 1574 (m; C=C_{ar}), 817 (m; C–H_{ar}), 764 (m; C–H_{ar}) and 693 (s; C–H_{ar}). UV−vis [1.0 x 10^{-5} M, CH_2Cl_2; λ_{max}, nm (ε, $M^{-1} \cdot cm^{-1}$)]: 274 (1.2 × 10^5), 314 (8.3 × 10^4), 457 (8.2 × 10^4), 722 (8.2 × 10^3). Anal. calc. for $C_{112}H_{92}F_{12}N_4O_{20}Ru_4S_4$ (2572.46): C 52.24, H 3.61, N 2.18; Found: C 52.45, H 3.81, N 2.22.

[Ru_4(η^6-*p*-cymene)$_4$(μ^4-donq)$_2$(μ^2-L_4)$_2$][CF_3SO_3]$_4$ (A_9): Green solid (570 mg, 82%). ^{1}H-NMR ($(CD_3)_2CO$, 400 MHz): δ 8.72 (s, 4H), 8.55 (d, *J* =6.8 Hz, 4H), 8.48 (d, *J* = 5.6 Hz, 4H), 8.01 (dd, *J* = 6.4 Hz and *J* = 2.8 Hz, 8H), 7.62 (t, *J* = 6.8 Hz, 4H), 7.48 (dd, *J* = 6.8 Hz and *J* = 3.2 Hz, 8H), 7.44 (s, 8H), 6.09 (d, *J* = 6.0 Hz, 8H), 5.86 (d, *J* = 6.0 Hz, 8H), 3.04 (sept, *J* = 6.8 Hz, 4H), 2.26 (s, 12H), 1.42 (d, *J* = 6.8 Hz, 24H). ^{13}C{^{1}H}-NMR

($(CD_3)_2CO$, 100 MHz): δ 154.9 (4C), 152.7 (4C), 142.4 (4C), 138.6 (8C), 133.0 (4C), 131.8 (8C), 128.3 (8C), 127.0 (8C), 126.8 (4C), 122.9 (4C), 117.7 (4C), 112.4 (8C), 109.3 (4C, C $_{CF3SO3}$), 104.4 (4C), 100.9 (4C), 97.2 (4C), 91.7 (4C), 85.5 (8C), 83.72 (8C), 31.62 (4C), 22.48 (8C), 17.43 (4C). *D*($(CD_3)_2CO$): 6.80 x 10^{-10} $m^2 \cdot s^{-1}$. IR (cm^{-1}): 2971 (w; C–H_{ar}), 2204 (w; C≡C), 1531 (m; C=C_{ar}), 967 (m; C–H_{ar}), 852 (m; C–H_{ar}), 763 (m; C–H_{ar}), 635 (s, sharp; C–H_{ar}). UV−vis [1.0 x 10^{-5} M, CH_2Cl_2; λ_{max}, nm (ε, $M^{-1} \cdot cm^{-1}$)]: 271 (1.8 × 10^5), 310 (9.0 × 10^4), 445 (9.1 × 10^4), 476 (6.7 × 10^4), 694 (1.9 × 10^4). Anal. calc. for $C_{120}H_{96}F_{12}N_4O_{20}Ru_4S_4$ (2674.72): C 53.88, H 3.63, N 2.08; Found: C 53.69, H 3.59, N 2.15.

*2.3.2. General procedure for the synthesis of dinuclear ruthenium(II) complexes with anthracenyl derivatives (**A_{10} – A_{13}**).*

The complex [Ru(η^6-*p*-cymene)(pta)Cl_2] (100 mg, 0.22 mmol) and silver trifluoromethanesulfonate (55 mg, 0.22 mmol) was dissolved in CH_2Cl_2 (10 mL) and stirred for 3 h at room temperature. The mixture was filtrated in order to eliminate silver chloride. The resulting solution was added to a CH_2Cl_2 solution containing the anthracene ligand (**L_1-L_4**, 0.11 mmol). Then, the mixture was refluxed overnight and consequently concentrated under vacuum. The concentrated solution was slowly poured into cold Et_2O and/or pentane to induce precipitation. After filtration, the dinuclear assemblies were dried under vacuum.

[{Ru(η^6-*p*-cymene)(pta)Cl}$_2$(μ^2-L_1)][CF_3SO_3]$_2$ (A_{10}): Yellow solid (142 mg, 87%). ^{1}H-NMR (CD_3CN, 400 MHz): δ 8.97 (m, 4H), 7.64 (m, 4H), 7.60 (m, 4H), 7.52 (m, 4H), 5.93 (m, 8H), 4.60 (m, 12H), 4.31 (m, 12H), 2.67 (sept, *J* = 6.8 Hz, 2H), 2.09 (s, 6H), 1.31 (d, *J* = 6.8 Hz, 6H), 1.17 (d, *J* = 7.2 Hz, 6H). $^{13}C\{^1H\}$-NMR (CD_3CN, 100 MHz): δ 157.5 (4C), 134.5 (2C), 129.8 (4C), 129.7 (2C), 127.8 (4C), 126.9 (4C),123.7 (4C), 111.0 (2C), 101.4 (2C), 91.5 (2C), 89.7 (2C), 89.5 (2C), 85.6 (2C), 73.3 (3C), 73.2 (3C),

52.1 (3C), 52.0 (3C), 31.9 (2C), 22.5 (2C), 22.4 (2C), 18.6 (2C). *D*(CD_3CN): 5.85 x 10^{-10} $m^2 \cdot s^{-1}$. IR (cm^{-1}): 3070 (w; C–H_{ar}), 2938 (w; C–H_{ar}), 1609 (m; C=C_{ar}), 1255 (s; C=C_{ar}), 1155 (m; C=C_{ar}), 1028 (s; C=C_{ar}), 637 (s; C–H_{ar}). ESI–MS (+); $[M\text{-}2(CF_3SO_3)^-]^{2+}$ *exp.* 594.1256 found. 594.1252. UV−vis [1.0 x 10^{-5} M, CH_3CN; λ_{max}, nm (ε, $M^{-1} \cdot m^{-1}$)]: 359 (1.3 × 10^4), 377 (1.8 × 10^4), 399 (3.0 × 10^4), 439 (2.2 × 10^4).

[{Ru(η^6-*p*-cymene)(pta)Cl}$_2$(μ^2-L_2)][CF_3SO_3]$_2$ (A_{11}): Yellow solid (113 mg, 69%). ^{1}H-NMR (CD_3CN, 400 MHz): δ 8.91 (m, 4H), 8.17 (d, *J* = 8 Hz, 2H), 7.86 (m, 2H), 7.58 (m, 8H), 5.89 (m, 8H), 4.59 (m, 12H), 4.24 (m, 12H), 2.58 (sept, *J* = 6.4 Hz, 2H), 2.01 (m, 6H), 1.15 (m, 12H). $^{13}C\{^1H\}$-NMR (CD_3CN, 100 MHz): δ 157.8 (1C), 157.0 (1C), 150.0 (2C), 143.2 (2C), 137.7 (2C), 133.1 (2C), 130.9 (2C), 129.8 (1C), 129.6 (1C), 127.7 (1C), 127.6 (1C), 127.5 (1C), 127.4 (1C), 127.2 (1C), 127.0 (1C), 126.9 (1C), 124.8 (1C), 123.7 (1C), 120.7 (1C), 113.0 (2C), 101.3 (2C), 91.2 (1C), 89.6 (1C), 89.5 (1C), 89.4 (1C), 89.3 (1C), 89.2 (1C), 85.7 (1C), 85.6 (1C), 73.3 (3C), 73.2 (3C), 52.2 (3C), 52.0 (3C), 31.9 (1C), 31.7 (1C), 22.4 (1C), 22.3 (1C), 22.2 (1C), 22.1 (1C), 18.6 (1C), (1C). *D*(CD_3CN): 5.49 x 10^{-10} $m^2 \cdot s^{-1}$. IR (cm^{-1}): 3071 (w; C–H_{ar}), 2936 (w; C–H_{ar}), 1608 (m; C=C_{ar}), 1257 (s; C=C_{ar}), 1155 (m; C=C_{ar}), 1028 (s; C=C_{ar}), 636 (s; C–H_{ar}). ESI–MS (+); $[M\text{-}2(CF_3SO_3)^-]^{2+}$ *exp.* 594.1256 found. 594.1252. m/z = 594.6 $[M\text{-}2(CF_3SO_3)]^{2+}$, 760.2 [M-{Ru(*p*-cymene)(pta)Cl}-2(CF_3SO_3)]$^+$, 1337.2 [M-(CF_3SO_3)]$^+$. UV−vis [1.0 x 10^{-5} M, CH_3CN; λ_{max}, nm (ε, $M^{-1} \cdot m^{-1}$)]: 357 (1.4 × 10^4), 376 (1.9 × 10^4), 399 (3.0 × 10^4), 441 (1.1 × 10^4).

[{Ru(η^6-*p*-cymene)(pta)Cl}$_2$(μ^2-L_3)][CF_3SO_3]$_2$ (A_{12}): Dark yellow solid (93 mg, 55%). ^{1}H-NMR (CD_3CN, 400 MHz): δ 8.68 (m, 4H), 8.47 (d, *J* = 16.4 Hz, 1H), 8.39 (m, 4H), 8.31 (d, *J* = 16.4 Hz, 1H), 7.74 (m, 4H), 7.58 (m, 4H), 7.06 (d, *J* = 16.8 Hz, 1H), 6.97 (d, *J* = 16.4 Hz, 1H), 5.83 (m, 8H), 4.56 (m, 12H), 4.22 (m, 12H), 2.60 (sept, *J* = 7 Hz, 2H), 2.00 (s, 6H), 1.20 (m, 12H). *D*(CD_3CN): 6.09 x 10^{-10} $m^2 \cdot s^{-1}$. IR (cm^{-1}): 3065 (w; C–

H_{ar}), 2940 (w; C–H_{ar}), 1607 (m; C=C_{ar}), 1257 (s; C=C_{ar}), 1155 (m; C=C_{ar}), 1029 (s; C=C_{ar}), 637 (s; C–H_{ar}). ESI–MS (+); $[M\text{-}2(CF_3SO_3)^-]^{2+}$ *exp.* 620.1413 found 620.1422. UV−vis [1.0 x 10^{-5} M, CH_3CN; λ_{max}, nm (ε, $M^{-1}\cdot m^{-1}$)]: 442 (5.1 × 10^4), 384 (1.3 × 10^4), 470 (3.6 × 10^4).

[{Ru(η^6-*p*-cymene)(pta)Cl}$_2$(μ^2-L_4)][CF_3SO_3]$_2$ (A_{13}): Orange solid (130 mg, 77%). ^{1}H-NMR (CD_3CN, 400 MHz): δ 8.92 (d, *J* = 5.6 Hz, 2H), 8.73 (s, 1H), 8.17 (d, *J* = 8.4 Hz, 2H), 7.61 (d, *J* = 6 Hz), 7.58 (s, 1H), 7.52 (m, 8H), 5.78 (m, 8H), 4.56 (m, 12H), 4.28 (m, 12H), 2.65 (sept, *J* = 7.1 Hz, 2H), 2.06 (s, 6H), 1.30 (d, *J* = 6.8 Hz, 6H), 1.16 (d, *J* = 7.2 Hz, 6H). ^{13}C{^{1}H}-NMR (CD_3CN, 100 MHz): δ 157.1 (2C), 151.6 (1C), 150.6 (1C), 144.9 (2C), 132.1 (2C), 132.0 (2C), 129.9 (1C), 129.8 (1C), 129.6 (1C), 129.5 (1C), 129.4 (1C), 128.5 (1C), 127.7 (1C), 127.3 (1C), 127.1 (1C), 126.6 (1C), 126.5 (1C), 126.3 (1C), 126.0 (1C), 110.8 (2C), 101.1 (1C), 100.8 (1C), 96.8 (2C), 95.8 (2C), 91.2 (2C), 89.5 (2C), 89.2 (2C), 88.7 (2C), 73.1 (3C), 73.0 (3C), 52.8 (1C), 52.6 (1C), 52.1 (2C), 52.0 (2C), 31.8 (1C), 31.7 (1C), 22.4 (1C), 22.3 (1C), 22.2 (1C), 22.0 (1C), 18.5 (2C). *D*(CD_3CN): 6.57 x 10^{-10} $m^2\cdot s^{-1}$. IR (cm^{-1}): 3057 (w; C–H_{ar}), 2940 (w; C–H_{ar}), 2385 (w; C≡C), 1609 (m; C=C_{ar}), 1259 (s; C=C_{ar}), 1156 (m; C=C_{ar}), 1029 (s; C=C_{ar}), 367 (s; C–H_{ar}). ESI–MS (+); $[M\text{-}2(CF_3SO_3)^-]^{2+}$ *exp.* 620.1413 found 620.1422. UV−vis [1.0 x 10^{-5} M, CH_3CN; λ_{max}, nm (ε, $M^{-1}\cdot m^{-1}$)]: 371 (1.7 × 10^4), 385 (1.9 × 10^4), 396 (2.6 × 10^4), 444 (8.3 × 10^3).

*2.3.3. General procedure for the synthesis of mononuclear ruthenium(II) complexes with anthracene derivatives (**A_{14}** – **A_{15}**).*

The complex [Ru(η^6-*p*-cymene)(pta)Cl_2] (50 mg, 0.11 mmol) and silver trifluoromethanesulfonate (28 mg, 0.11 mmol) was dissolved in CH_2Cl_2 (5 mL) an stirred for 3 h at room temperature. The mixture was filtrated in order to eliminate silver chloride. The resulting solution was added to a CH_2Cl_2 solution containing the

anthracene ligand (**L_6** or **L_7**, 0.11 mmol). Then, the mixture was refluxed overnight and consequently concentrated under vacuum. The concentrated solution was slowly poured into cold pentane to induce precipitation. After filtration, the mononuclear assemblies were dried under vacuum.

[{Ru(η^6-*p*-cymene)(pta)Cl}(μ^2-L_6)][CF_3SO_3] (A_{14}): yellow solid (71 mg, 78%). ^{1}H-NMR (CD_3CN, 400 MHz): δ 8.91 (d, *J* = 6 Hz, 1H), 8.74 (m, 2H), 8.19 (t, *J* = 7 Hz, 2H), 8.12 (d, *J* = 8 Hz, 1H), 7.78 (t, *J* = 6.4 Hz, 1H), 7.51 (m, 6H), 5.73 (m, 4H), 4.54 (m, 6H), 4.20 (m, 6H), 2.54 (sept, *J* = 7 Hz, 1H), 1.96 (s, 3H), 1.17 (d, *J* = 6.6 Hz, 3H), 1.09 (d, *J* = 6.8 Hz, 3H). ^{13}C{^{1}H}-NMR (CD_3CN, 100 MHz): δ 157.1 (1C), 155.5 (1C), 142.2 (1C), 137.1 (1C), 131.3 (1C), 130.2 (4C), 128.8 (1C), 128.7 (1C), 128.6 (1C), 126.7 (2C), 126.2 (2C), 125.6 (1C), 125.2 (2C), 111.5 (1C), 100.3 (1C), 90.0 (1C), 88.3 (1C), 84.9 (2C), 72.3 (2C), 72.2 (1C), 51.2 (2C), 51.1 (1C), 30.7 (1C), 21.4 (1C), 21.2 (1C), 17.6 (1C). *D*(CD_3CN): 6.57 x 10^{-10} $m^2 \cdot s^{-1}$. IR (cm^{-1}): 3057 (w; C–H_{ar}), 2940 (w; C–H_{ar}), 1444 (w; C=C_{ar}), 1257 (s; C=C_{ar}), 1156 (m; C=C_{ar}), 1029 (s; C=C_{ar}), 659 (s; C–H_{ar}). ESI–MS (+); [M-(CF_3SO_3)$^-$]$^+$ *exp.* 683.1644 found 683.1612. UV−vis [1.0 x 10^{-5} M, CH_3CN; λ_{max}, nm (ε, $M^{-1} \cdot m^{-1}$)]: 370 (1.4 × 10^4), 388 (1.5 × 10^4), 398 (2.2 × 10^4).

[{Ru(η^6-*p*-cymene)(pta)Cl}(μ^2-L_7)][CF_3SO_3] (A_{15}): yellow solid (42 mg, 45%). ^{1}H-NMR (CD_3CN, 400 MHz): δ 8.68 (d, *J* = 6.4 Hz, 2H), 8.59 (s, 1H), 8.48 (d, *J* = 16.4 Hz, 1H), 8.34 (m, 2H), 8.12 (m, 2H), 7.78 (d, *J* = 6.2 Hz, 2H), 7.56 (m, 4H), 7.09 (d, *J* = 16.8 Hz, 1H), 5.87 (m, 4H), 4.58 (m, 6H), 4.19 (m, 6H), 2.60 (sept, *J* = 6.8 Hz, 1H), 2.00 (s, 3H), 1.27 (m, 3H), 1.13 (d, *J* = 7.2 Hz, 3H). ^{13}C{^{1}H}-NMR (CD_3CN, 100 MHz): δ 157.1 (2C), 147.4 (1C), 134.7 (1C), 133.9 (1C), 132.4 (1C), 131.7 (1C), 130.2 (1C), 129.9 (2C), 128.9 (1C), 127.3 (2C), 126.6 (2C), 126.3 (2C), 124.3 (2C), 116.4 (1C), 109.9 (1C), 91.5 (1C), 89.1 (2C), 85.8 (1C), 73.1 (3C), 51.5 (3C), 31.9 (1C), 22.5 (1C), 22.2 (1C), 18.6 (1C). *D*(CD_3CN): 6.86 x 10^{-10} $m^2 \cdot s^{-1}$. IR (cm^{-1}): 3064 (w; C–H_{ar}), 2942

(w; C–H_{ar}), 1609 (m; C=C_{ar}), 1253 (s; C=C_{ar}), 1156 (m; C=C_{ar}), 1027 (s; C=C_{ar}), 637 (s; C–H_{ar}). ESI–MS (+); $[M-(CF_3SO_3)^-]^+$ *exp.* 683.1644 found 683.1669.. UV−vis [1.0 x 10^{-5} M, CH_3CN; λ_{max}, nm (ε, $M^{-1}\cdot m^{-1}$)]: 371 (1.0 × 10^4), 396 (2.0 × 10^4), 342 (3.5 × 10^4).

2.4. Mass Spectrometric Experiments

Unless stated otherwise, measurements were performed with 10 µM samples in acetonitrile and were injected with a flow rate of 2 µL/min. Ionization conditions were optimized for each sample, but typical settings were a capillary voltage of 2.25 kV, source and desolvation temperatures both set to 40°C, a sample cone voltage of 5 V and a source offset of 5 V. Collision-induced dissociation and ion mobility measurements were completed with N_2 as the collision and drift gases, respectively.

2.5. Photooxygenation of L_1-L_7 and the corresponding assemblies A_1-A_{15}

Stock solutions of **L_{anthr}** (**L_1**-**L_7**; 10^{-3} M; 2 mL) and tetrapyridylporphyrin (TPP) (1.10^{-4} M; 2 mL) were prepared in CH_2Cl_2 while stock solutions of **A_{anthr}** (**A_1**-**A_{15}**; 10^{-3} M; 2 mL) were prepared in CH_3CN, both solvents were firstly degassed with three freeze-pump-thaw cycles. The different samples were prepared by mixing TPP (250 µL) and **L_{anthr}** or **A_{anthr}** (500 µL). Each sample has a final concentration in CH_2Cl_2 of TPP of 1.10^{-5} M and **L_{anthr}** or **A_{anthr}** of 5.10^{-5} M.

Photooxygenation was done on each sample by first bubbling O_2 in a closed vial for 30 seconds and then by irradiating with a white lamp in a photoreactor. In order to follow the kinetics of the photooxygenation, measurements were recorded at 0, 30, 60, 90, 120, 150, 180, 240, 300, 360, 420, 480, 540, 600, 720, 840, 960, 1200, 1500, 1800, 2100, 2400, 3000 seconds. ^{1}H NMR were also completed to follow the formation of endoperoxides (before irradiation and after 15 h reaction time).

2.6. Cell culture

2.6.1. Instrumentation and methods

All manipulations were carried out under an inert atmosphere and strict sterilization conditions. DU145 prostatic cancer cells were provided by the American Type Culture Collection (LGC Standards, Middlesex, UK). 3-(4,5-dimethylthiazol-2-yl)-2,5-diphenyltetrazoliumbromide (MTT) and L-glutamine were purchased from Sigma-Aldrich (Steinheim, Germany). Dimethyl sulfoxide (DMSO) were purchased from Acros Organics (New Jersey, USA). RPMI-1640, fetal bovine serum (FBS) and penicillin/streptomycin were purchased from Gibco BRL (Cergy-Pontoise, France). The organometallic complexes and organic compounds were dissolved at 1 mM in DMSO as the stock solution and then diluted in complete medium to the required concentration immediately preceding to use. DMSO concentrations used were always < 0.1 %. Cell irradiation was carried out using a red light source of 630 nm, 75 J/cm^2, CureLight®, PhotoCure ASA. Absorbance after MTT assay was measured by Dynex Triad Multi Mode Microplate Reader, Dynex Technologies, Germany.

2.6.2. Cell culture

DU145 cells were grown in a 75 cm^2 culture plate in RPMI complete medium containing 10 % of FBS, 5 % of L-glutamine and 5 % of penicillin/streptomycin. The culture medium was renewed every 2 days. Cells were subcultured by dispersal with trypsin-EDTA and replated at 7.5 x 10^5 cells/ml in fresh medium.

2.7. Photocytotoxicity on DU145 Prostatic cancer cells

DU145 prostatic cancer cells were plated in 96-well plates (7000 cells/100 µl per well) and incubated in the dark in complete medium for 24 h, maintained at 37 °C in humidified atmosphere with 5 % CO_2. Then, 100 µl of medium with different

concentrations of ruthenium complexes (10, 100, 250, 500, 750 and 1000 nM) and TPP (1/5 of concentrations of the complex) were added, maintained 24 h at 37 °C in humidified atmosphere with 5% CO_2. After 24 h, the medium was removed and replaced by medium without red phenol containing 10 % FBS, 5 % of L-glutamine and 5 % of penicillin/streptomycin. Cells were irradiated at 40 mW/cm^2 for 30 minutes (wavelength 630 nm). Cell survival was tested by MTT assay 24 h after, using 10 µL of MTT per well. After 4 h, the medium was removed and 200 µL of DMSO were added to each well.

3. Results and discussion

3.1. Synthesis and characterization of mononuclear, dinuclear and tetranuclear complexes A_1-A_{15}

The general synthetic strategy is described in Fig. 3. Two parts are forming the final arene ruthenium(II) assemblies (or $\mathbf{A_{anthr}}$), the ruthenium clip(s) and the organic linker(s) respectively. The organic linkers built from anthracenyl-derivatives ($\mathbf{L_1}$-$\mathbf{L_7}$) are used to capture oxygen. For the metalla-rectangles, three types of OO∩OO spacers between two ruthenium atoms were selected for the clips, oxalato (**oxa**), dihydroxybenzoquinonato (**dobq**) and dihydroxynaphthoquinonato (**donq**), thus forming the corresponding metalla-clips $[Ru_2(\eta^6\text{-}p\text{-cymene})_2(\mu^4\text{-oxa})Cl_2]$, $[Ru_2(\eta^6\text{-}p\text{-cymene})_2(\mu^4\text{-dobq})Cl_2]$, $[Ru_2(\eta^6\text{-}p\text{-cymene})_2(\mu^4\text{-donq})Cl_2]$ (respectively named **Ru-oxa**, **Ru-dobq** and **Ru-donq**) [31-33]. The mononuclear complex $[Ru(\eta^6\text{-}p\text{-cymene})(pta)Cl_2]$ (**Ru-PTA**) was also synthetized in order to, first, provide other types of arene ruthenium(II) structures (mono- and dinuclear complexes), and second, to increase the solubility of the corresponding $\mathbf{A_{anthr}}$ in water and polar organic solvents, which can be very convenient for biological applications [34]. The pyridinyl-anthracenyl ligands ($\mathbf{L_{anthr}}$) were obtained via different palladium-catalyzed cross-coupling reactions (Suzuki, Heck or Sonogashira). As shown in Fig. 3, the structures of $\mathbf{L_1}$-$\mathbf{L_7}$ differ from each other by a different electronic repartition around the $^1O_2$ capture unit, thanks to single, double or triple bond(s) between the anthracenyl and the pyridyl units. Except for $\mathbf{L_6}$, all the characterizations were previously published (supporting information, part 1) [36-40].

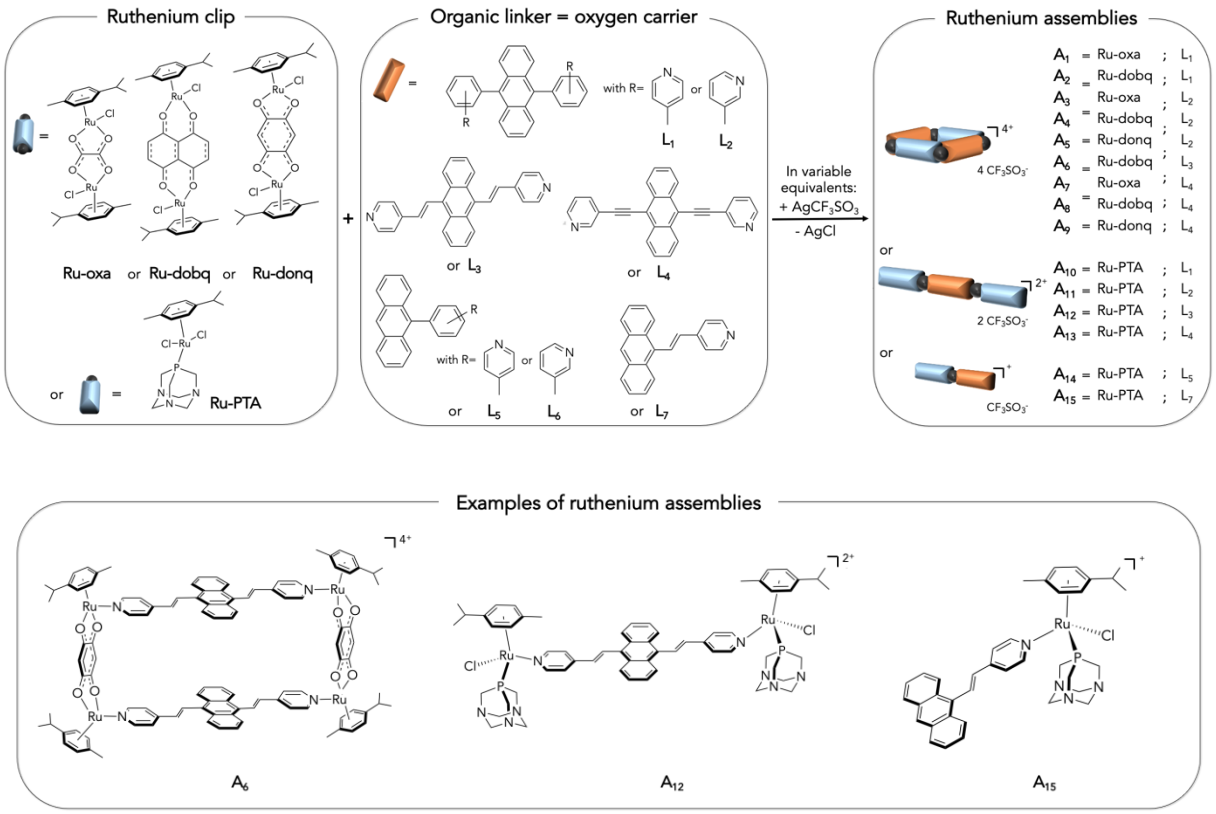

Fig. 3. General synthetic strategy to afford ruthenium assemblies **A_1**-**A_{15}**. Three examples of synthetized complexes (**A_6**, **A_{12}** and **A_{15}**) are also drawn.

Crystals of **L_6** were obtained by slow evaporation of a CH_2Cl_2/EtOAc (4/1) solution, and the crystallographic data confirm its molecular structure (Fig. 4a and supporting information, part 2). **L_6** crystallized in the monoclinic centrosymmetric space group *P* $2_1/c$. In the crystal, the angle between the plane of the anthracenyl and the plane of the pyridyl unit is almost orthogonal (blue and orange, in Fig. 4b). This is reflected by the value of the angle between the two planes which is 103.11°. This configuration is probably due to an optimization of the electronic density repartition within the molecule, since the nitrogen atom is in a *meta* position from the anthracenyl core.

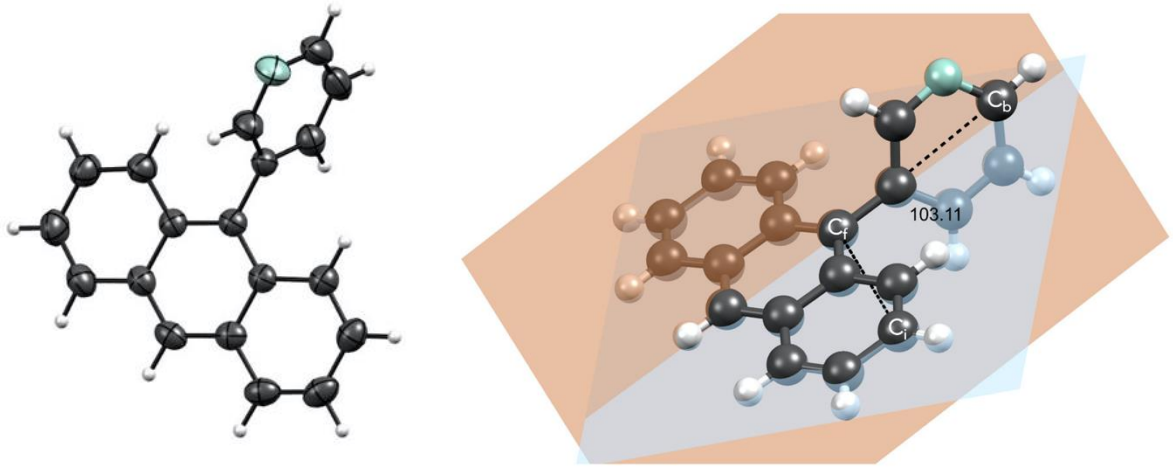

Fig. 4. (a) ORTEP drawing of **L_6** at 50% probability level ellipsoids; (b) Crystallographic structure of **L_6** with two planes: one containing the anthracenyl core (in blue) and one corresponding to the pyridyl group (in orange).

Different mono-, di- and tetranuclear ruthenium(II) complexes (**A_1**-**A_{15}**) were synthesized from **L_1**-**L_7** (Fig. 3). In order to determine the influence of the ruthenium atoms composing the assembly and the possible presence of π-π stacking interactions between two anthracenyl units in the tetranuclear assemblies (**A_1**-**A_9**), which can overall hamper its ability to capture oxygen (Fig. 3), mononuclear and dinuclear analogues were also prepared. All cationic *p*-cymene ruthenium(II) derivatives **A_1**-**A_{15}** were isolated as their trifluoromethanesulfonate salts, in yields ranging from 39% to 87%. The final color is generally linked to the ruthenium(II) precursors: yellow for **Ru-oxa**, red for **Ru-dobq**, green for **Ru-donq** and yellow-orange for **Ru-PTA**. The solubility of the assemblies depends on the nature of the ruthenium(II) precursors: **A_3** and **A_7** are both soluble in ethanol and slightly in dichloromethane, while the others (**A_1**-**A_2**; **A_4**-**A_6** and **A_8**-**A_{15}**) show an opposite tendency. However, they are all soluble in acetone and in acetonitrile. Elemental analyzes were consistent with theoretical calculated values for three rectangles (**A_7**, **A_8**, **A_9**). Despite several purifications (precipitation in diethyl ether and in pentane) and a long drying period, using a vacuum

pump (about 10^{-3} mbar), the other elemental analyses were not accurate. Such systems tend to trap solvent molecules in their cavity [41], which appears to be the case here. Nevertheless, the structures of the metalla-assemblies were confirmed by NMR and mass spectrometry (experimental part).

^{1}H NMR spectra of $\mathbf{A_{anthr}}$ show typical peak multiplicities and chemical shifts of the arene ruthenium(II) units. For example, depending on the assembly, aryl protons of the *p*-cymene are present around 5.65 and 6.65 ppm; isopropyl protons at around 1.25-1.45 ppm; methyl protons at 1.95-2.35 ppm; or two multiplets for the CH_2 groups from the pta group (at respectively around 4.20 ppm and 4.55 ppm). $\mathbf{A_{anthr}}$ also display peaks for $\mathbf{L_{anthr}}$, that did not significantly shift. Interestingly, except for $\mathbf{A_6}$, $\mathbf{A_8}$ and $\mathbf{A_9}$, the majority of the tetranuclear complexes has broad signals in the aromatic region and additional splitting of some protons from the *p*-cymene unit. Such observation strongly suggests the formation of two isomers, *cis* and *trans*, with similar signal patterns, which is consistent with analogous tetranuclear arene ruthenium assemblies.

The formation of $\mathbf{A_{anthr}}$ was also confirmed by electrospray mass spectrometry (ESI-MS). The spectra show the expected isotope patterns of arene ruthenium(II) assemblies with ionisation coming from stripping of trifluoromethanesulfonate ($CF_3SO_3^-$) counterions (Table S2). However, the assemblies also undergo facile fragmentation producing peaks corresponding to cleavage of the $\mathbf{L_{anthr}}$-Ru bond, loss of the clip and/or the *p*-cymene ligand (methyl or isopropyl). The degree of fragmentation seems most prevalent with $\mathbf{L_4}$ and **donq** assemblies with intact assemblies not observed in those cases, whilst **dobq** seems to provide the greatest stability. Collision-induced dissociation (CID) measurements of $\mathbf{A_6}$ show that the predominate fragmentation pathway of the intact cage is cleavage of Ru-N bonds

(Figure S1, S2 & Scheme S1). The fragmentation of the mass-selected +4 charge state, for example, leads predominantly to doubly charged halves of the parent ion. This leads to superposition of parent and daughter ion signals as the +4 parent ion and the +2 daughter ion have the exact same m/z. This can be clearly seen from the isotopic patterns which indicates a +4 charge state prior and a +2 charge state after the fragmentation reaction. Already before ionization, the +2 fragment generated in the ion source contributes a minor fraction to the pattern so that the pattern deviates from the pattern calculated for the +4 parent ion.

Ruthenium(II) complexes $\mathbf{A}_{\mathbf{anthr}}$ were also characterized by UV-VIS spectroscopy. All measurements in the range of 250 and 700 nm were made at room temperature in a mixture of dichloromethane/acetonitrile (95/5), in order to dilute the metalla-complexes and to compare them under similar conditions. The intense high energy band centered at 270-330 nm is assigned to ligand π-π* transition and intra-ligand charge transfer (ILCT). They also display a broad low-energy band, which corresponds to metal-to-ligand charge transfer (MLCT). Anthracene units show characteristic bands in the UV-VIS spectra in the region around 300 and 550 nm. However, the absorption bands are usually broader than those observed in the spectra of the free anthracenyl-based ligands [42].

3.2. Photooxygenation studies

These studies are based on the comparison between the photooxygenation of $\mathbf{L}_{\mathbf{anthr}}$ and $\mathbf{A}_{\mathbf{anthr}}$. The main question is to determine whether the formation of metal-based assemblies and the presence of arene ruthenium(II) unit(s) enhance or decrease the reactivity towards $^1O_2$. Solutions of $\mathbf{L}_{\mathbf{anthr}}$ and $\mathbf{A}_{\mathbf{anthr}}$ were prepared just before the

experiments with solvents previously made oxygen-free by several cycles of freeze-pumping. For each sample, an external photosensitizer 5,10,15,20-tetra(4-pyridyl)-21*H*,23*H*-porphine (or TPP) was added to allow the reaction with oxygen. The ratio TPP/anthracene unit was 1/5. [30] A first measurement was made in an inert atmosphere and then compared to other measurements with an atmosphere saturated with oxygen, which was prepared by bubbling O_2 (0,5 Bar, 30 seconds) through the solution, and followed by a white light irradiation (400-800 nm; 8 W).

3.2.1. ^{1}H NMR studies.

The recording of ^{1}H NMR spectra of all $\mathbf{L_{anthr}}$ (1 mM; in CD_2CH_2) and $\mathbf{A_{anthr}}$ (1 mM; in CD_2CH_2/CD_3CN, variable proportions) was realized after 15 hours of irradiation. Except for $\mathbf{L_4}$, all the $\mathbf{L_{anthr}}$ were undoubtedly converted to some extend to their endoperoxide form (Fig. S1 and S2). These observations were expected since the experiments were based on previous studies [22, 24]. The most impacted signals by the [4+2] cycloaddition correspond to the protons around the binding site where singlet oxygen was inserted. This phenomenon was clearly seen for the proton at C(19) of the anthracenyl unit ($\mathbf{L_5}$, $\mathbf{L_6}$ and $\mathbf{L_7}$). This signal is usually displaced upfield by about 2 ppm (Fig. S2). These observations support the addition of oxygen on the anthracenyl core, which is translated in the ^{1}H NMR spectra into an upfield shift of the anthracenyl signals. Similar observations are expected when regarding $\mathbf{A_{anthr}}$. All ^{1}H NMR suggest the formation of their corresponding endoperoxide form. However, despite strong efforts to improve the resolution of these spectra, the appearance of shifted signals were weak, but enough to indicate their possible interaction with O_2. Nevertheless, further analyses were carried out to provide further evidence that oxygen can be captured by these arene ruthenium(II) assemblies.

3.2.2. UV-Vis studies.

Additional evidence for endoperoxide formation of **L_{anthr}** and **A_{anthr}** (respectively **L_{anthr}-EPO** and **A_{anthr}-EPO**) comes from UV/Vis spectroscopy. When the [4+2] cycloaddition of oxygen takes place, the aromaticity and the electronic density change, which also affects the electronic transitions and by extension, the UV-VIS profile. The addition of $^1O_2$ can thus be monitored by the extinction of the absorption band corresponding to the anthracenyl core (around 300 and 400 nm). For **L_{anthr}** (5.0×10^{-5} M in CH_2Cl_2), three profiles could be observed, which correspond to pyridinyl derivatives: four or five decreasing absorption bands in the spectral window were nicely distinguishable for the linkers containing one or several pyridyl group(s) (**L_1**, **L_2**, **L_5**, **L_6**); a less well-defined, but still decreasing, absorption bands in the same spectral windows for linkers with one or two (pyridin-4-yl)vinyl unit(s) (**L_3** and **L_7**); and no change for the ligand with ethynylpyridine groups (**L_4**). So, the endoperoxide formation should be efficient for all **L_{anthr}**, except for **L_4**. This last result was not surprising, as this phenomenon was already noticed and explained by Fudikar and Linker [43].

Concerning the metalla-assemblies (5.0×10^{-5} M), photooxygenations were realized in a mixture of dichloromethane/acetonitrile (95/5) in order to have high solubility. All the UV-Vis spectra are available in Figures S3 and S4. At first sight, a tendency appears for the set from **A_1** to **A_9**: when **Ru-oxa** is engaged in a tetranuclear structure, the complexes seem to be more sensitive to the irradiation (Fig. 5a-c). Moreover, only the **Ru-oxa** complex **A_7**, derived from the non-efficient ligand **L_4**, was impacted by the irradiation (Fig. 5d). Surprisingly, two isobestic points appeared during the first five minutes of the light exposition and followed by an important extinction of the whole absorption bands (Fig. 5e). Two hypotheses could be made concerning **A_7**: first, the presence of an isobestic point reveals the existence of two species in solution, which

suggests the formation of **A_7-EPO** and second, two successive phenomena may be the sign of two different reactions (among them, the oxygen capture). Regarding the other ruthenium precursors, both assemblies **Ru-dobq** and **Ru-donq** show similar behavior. The introduction of **Ru-PTA** units do not prevent the extinction of the absorption bands, except for **A_{12}**, which seemed to be unreactive to light and oxygen (Fig. S4). So, the UV-Vis observations further support the cycloaddition of $^1O_2$ on a majority of **A_{anthr}**, but it must be confirmed by additional analysis, such as by mass spectrometry (MS).

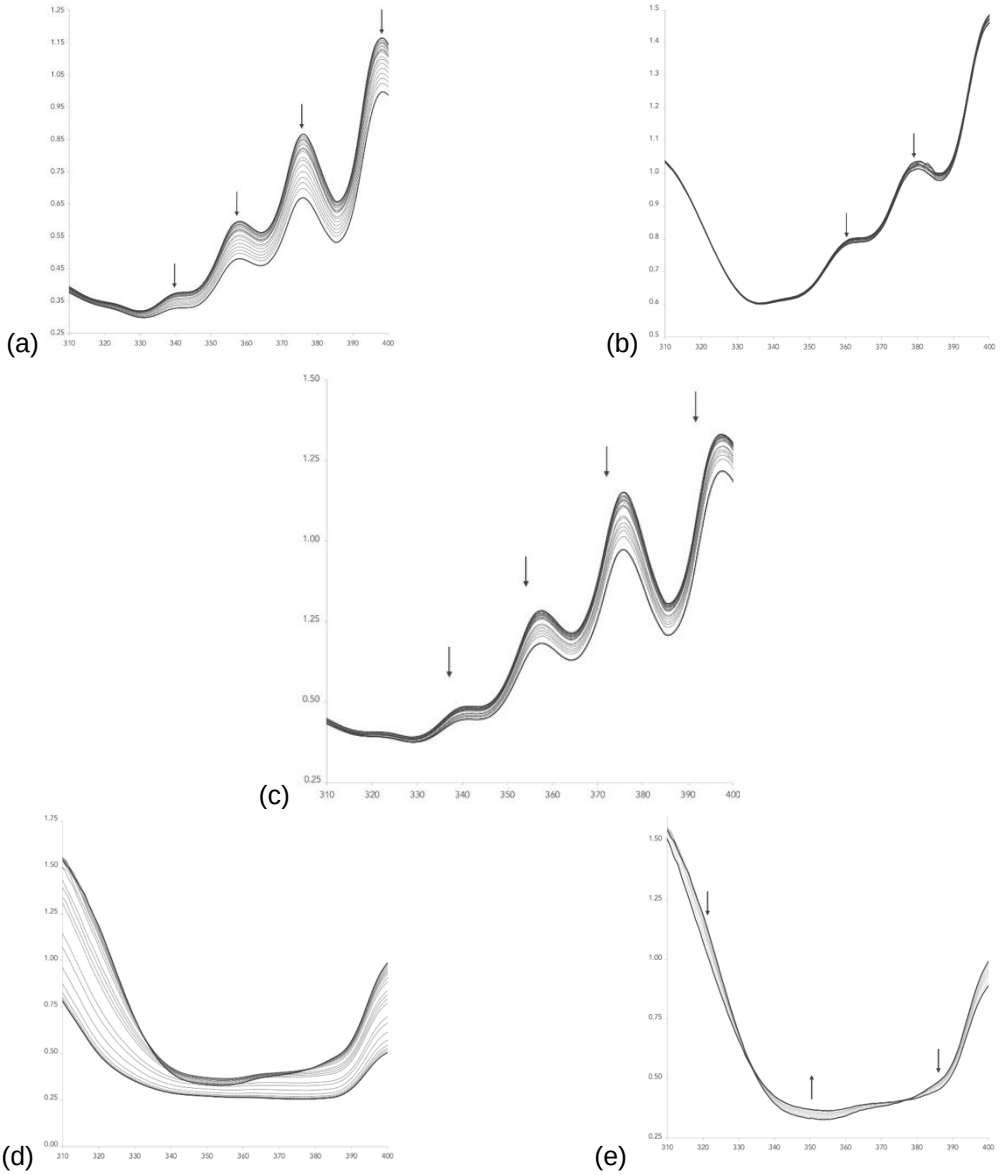

Fig. 5. UV-VIS spectra of **A_3** (a)**, A_4** (b)**, A_5** (c), at 5.0 x 10^{-5} M in CH_3CN/CH_2Cl_2 and during irradiation (white light; t = 0 to 60 min; with TPP). UV-VIS spectra of **A_7** (5.0 x 10^{-5} M in CH_2Cl_2/CH_3CN, 95/5) during

irradiation (white light; (d): t = 0 to 60 min and (e): t = 0 to 5 min).

3.2.3. Mass spectrometry studies.

Table 1: *m/z* values from ESI-MS spectra for **A_{anthr}-EPO.**

	ESI-MS peaks
A_1-EPO	$[M\text{-}4(CF_3SO_3^-)\text{-}O_2]^{4+}$: 478.6 $[M\text{-}3(CF_3SO_3^-)\text{-}O_2]^{3+}$: 677.1 $[M\text{-}2(CF_3SO_3^-)\text{-}O_2]^{2+}$: 1090.1
A_2-EPO	$[M\text{-}4(CF_3SO_3^-)\text{-}O_2$-arene-3methyl-3isopropyl$]^{4+}$: 431.9
A_3-EPO	$[M\text{-}4(CF_3SO_3^-)\text{-}O_2]^{4+}$: 474.1 $[M\text{-}3(CF_3SO_3^-)\text{-}O_2]^{3+}$: 633.3 $[M\text{-}4(CF_3SO_3^-)]^{4+}$: 487.1
A_4-EPO	$[M\text{-}3(CF_3SO_3^-)\text{-}O_2]^{3+}$: 688.1 $[M\text{-}2(CF_3SO_3^-)\text{-}O_2]^{2+}$: 1106.6 $[M\text{-}2(CF_3SO_3^-)]^{2+}$: 1123.1
A_5-EPO	$[M\text{-}3(CF_3SO_3^-)\text{-}O_2$-3arene-methyl$]^{3+}$: 583.1 $[M\text{-}4(CF_3SO_3^-)\text{-}O_2]^{4+}$: 504.6
A_6-EPO	$[M\text{-}4(CF_3SO_3^-)]^{4+}$: 513.2 $[M\text{-}2(CF_3SO_3^-)]^{2+}$: 1174.1
A_7-EPO	$[M\text{-}4(CF_3SO_3^-)\text{-}O_2]^{4+}$: 489.8
A_{10}-EPO	$[M+2H]^{2+}$: 760.2
A_{11}-EPO	$[M+2H]^{2+}$: 760.2
A_{15}-EPO	$[M\text{-}(CF_3SO_3^-)]^{+}$: 741.2

MS measurements were also performed to show the formation of **L_{anthr}-EPO** and **A_{anthr}-EPO**. Peaks corresponding to **L_{anthr}-EPO** could be seen when TPP was in the solution for all ligands except for **L_4** (Figure 6). The tetranuclear structures (**A_1**-**A_7**) displayed the same behavior with oxygenation occurring for solutions with TPP present (Figure 7 and table S2). Complexes **A_1**-**A_7** were able to capture two molecules of oxygen which is highly advantageous for PDT purposes. Oxygenated assemblies could not be seen for assemblies derived from **L_4**, as expected. This was also the case for the mono- or the dinuclear assemblies (**A_{10}**-**A_{15}**). CID measurements of doubly oxygenated **A_6** showed that the oxygen can be lost at low CID voltages before fragmentation of the assembly occurs (Figure S3). This suggest that the retro-[4+2]

cycloaddition already occurs at energies lower that those required for the fragmentation of the complex scaffold..

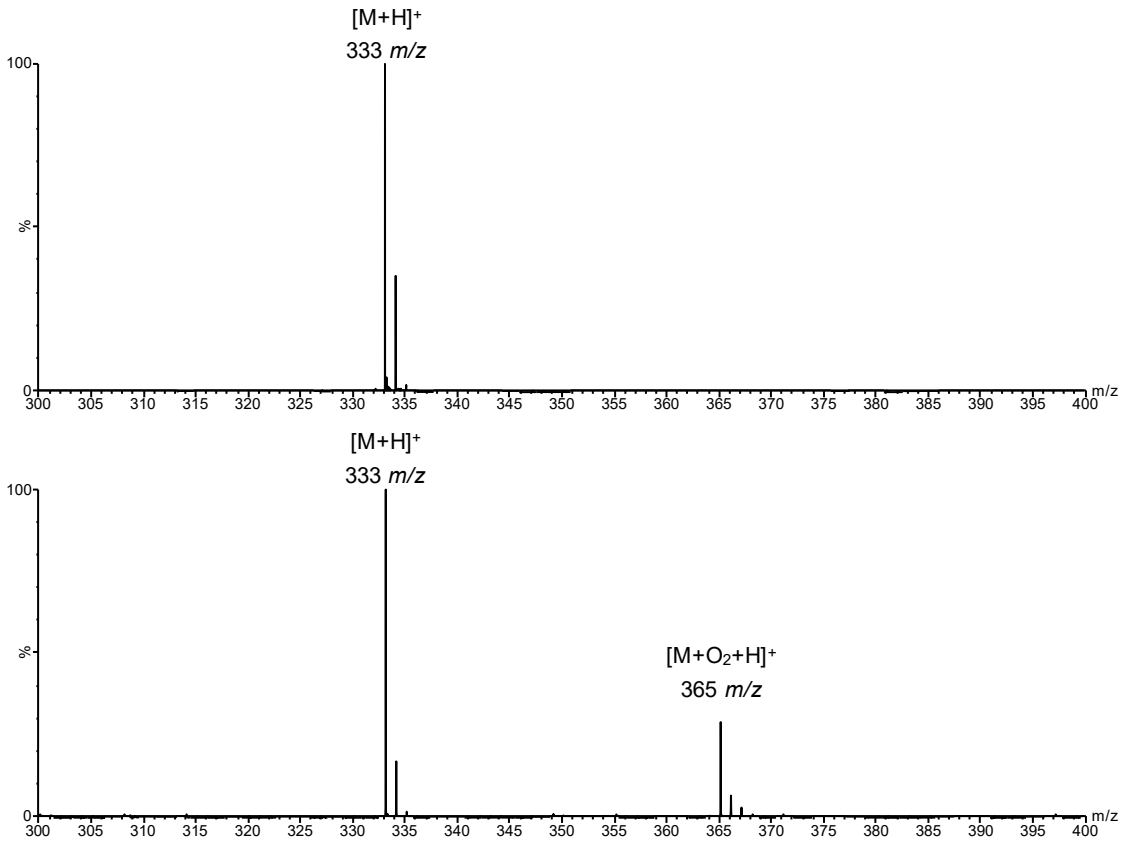

Fig. 6. TOF ESI-MS of ligand **L_1** without (top) and with TPP (bottom). **L_1-EPO** formation was only observed for samples with TPP.

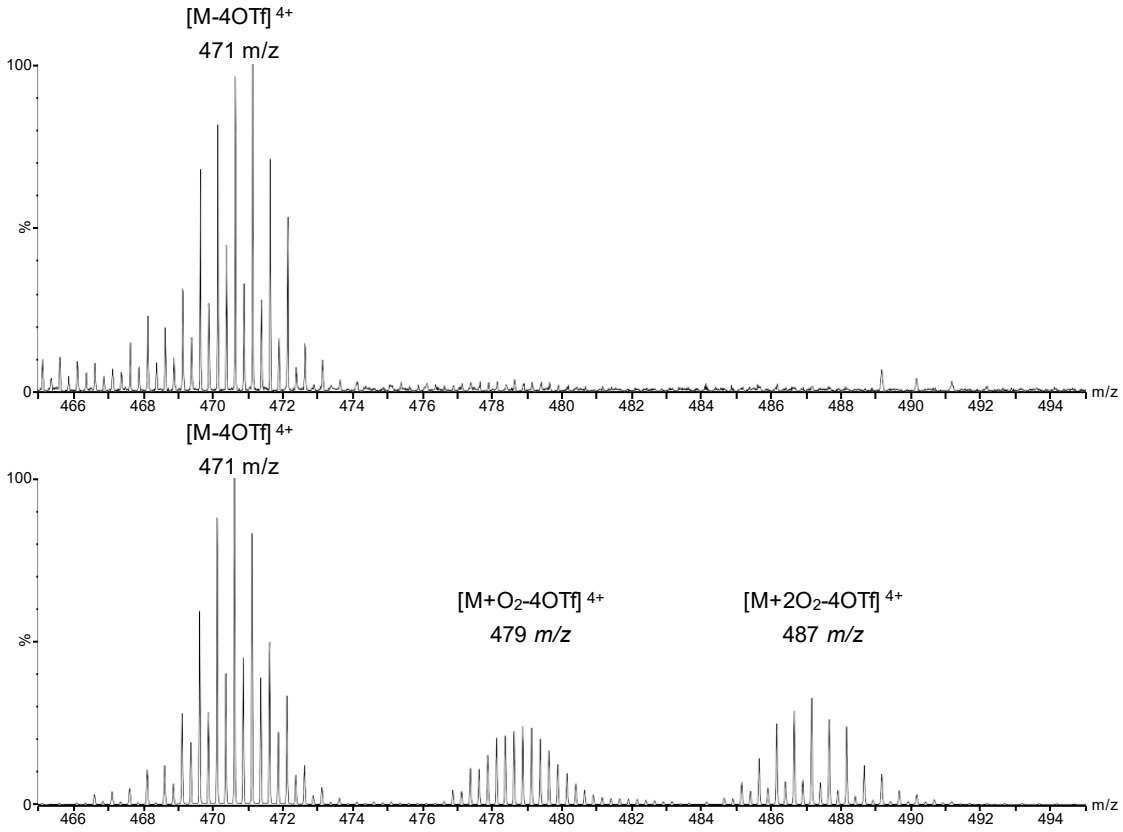

Fig. 7. TOF ESI-MS of assembly $\mathbf{A_1}$ with (a) and without (b) TPP. $\mathbf{A_1}$**-EPO** formation was only observed for samples with TPP. N.B The isotopic patterns show overlap of the +4 intact assembly and the +2 half.

During these measurements, it was surprisingly determined that oxygenation of $\mathbf{A_6}$ could occur without TPP. To investigate this, measurements were taken of a sample exposed to natural light and compared to a sample kept in the dark. These measurements showed the formation of the singly and doubly oxygenated species for the sample exposed to light whilst no oxygenation occurred for the dark sample. These results clearly show $\mathbf{A_6}$ to be able to act as a photosensitizer after exposure to natural light beyond its function as an oxygen trap and potential oxygen transporter. Such self-sensitizing behavior was not apparent for any other assembly.

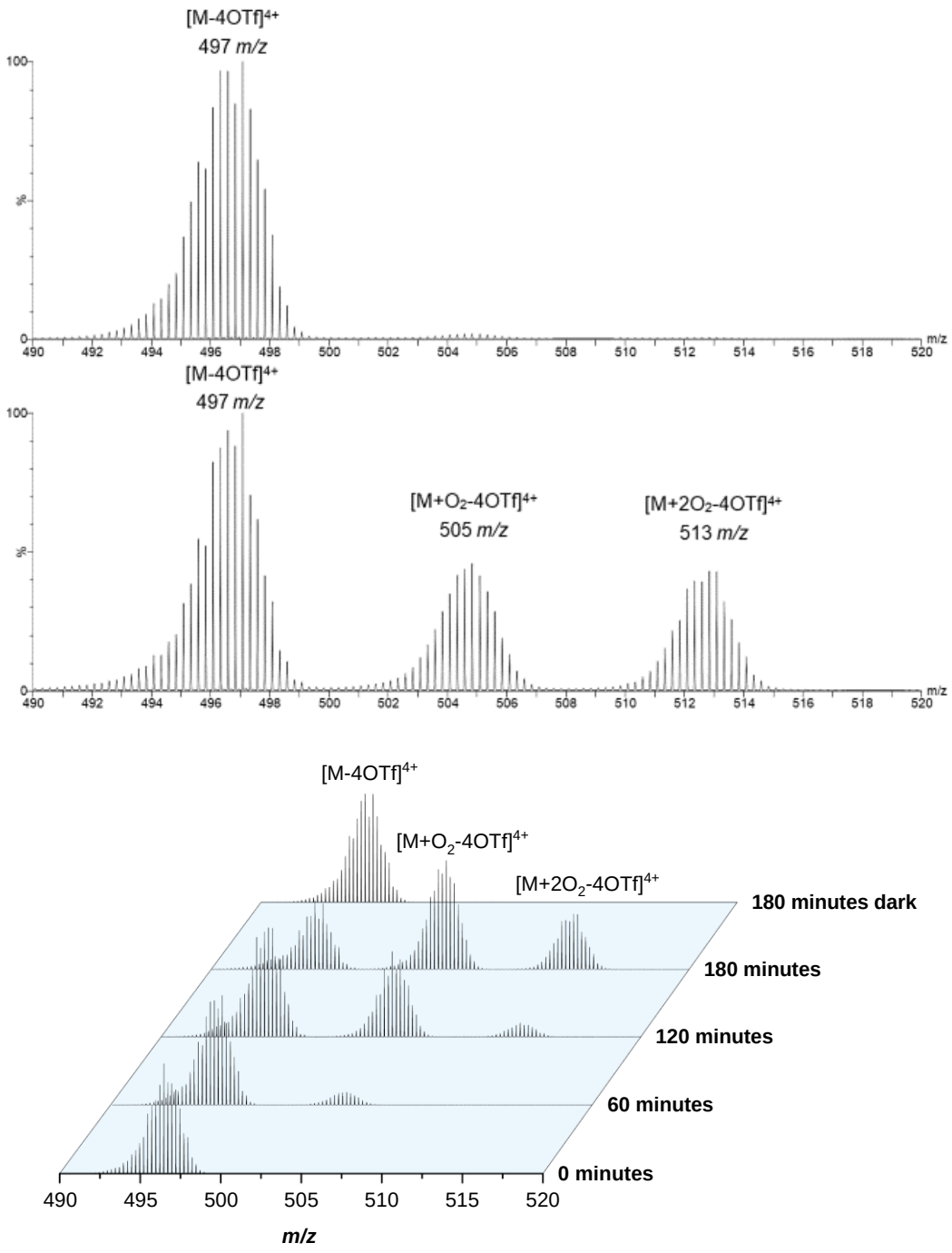

Fig. 7. TOF ESI-MS of **A_6** at several time points after exposure to natural light in the absence of the TPP sensitizer.

3.2.4. Kinetics studies of the photooxygenation of L_{anthr} and A_{anthr}.

After confirming that the majority of **A_{anthr}** are capable of capturing oxygen, it was important to determine whether the presence of the arene ruthenium and/or the formation of assemblies is a benefit or an impediment to the [4+2] cycloaddition. In that

perspective, the monitoring of the extinction of the absorption bands allowed us to determine the kinetics of the photooxygenation of $\mathbf{A}_{\mathbf{anthr}}$, compared to $\mathbf{L}_{\mathbf{anthr}}$, and to a reference commonly used in the literature, diphenylanthracene (DPA) [30,44]. We considered that the natural logarithm of the concentration of $\mathbf{L}_{\mathbf{anthr}}$ or $\mathbf{A}_{\mathbf{anthr}}$ over its initial concentration is proportional to the time. Therefore, the corresponding slopes (k') will give us the rate constants for each system (Table 2 and more details are available in the supporting information, part 3). The curves are shown in Fig. S5. The absolute second order rate constant (k) values were determined using the reference DPA (with a k value of 4.20×10^6 $M^{-1} \cdot s^{-1}$), to mathematically compare the different results [30,44]. The general assessment was clear: the presence of the arene ruthenium(II) in that kind of mono-, di- or tetranuclear structures penalizes the capture of oxygen by the anthracenyl moiety. The different isomers of the pyridinyl linkers did not show a distinct difference in the capture of oxygen when being incorporated into arene ruthenium complexes. In 2012, Fudickar and Linker suggested that the change of mechanistic pathway during the addition of O_2 could alter the feasibility of the reaction [43]. In fact, they explain this difference by the fact that the transitional molecule, corresponding to the interaction of O_2 with the anthracenyl core, is not stable enugh and then, favors a concerted more than a converted process. Since the concerted process is energetically unfavorable, the reaction is slower. This explanation can be also transposed to $\mathbf{A}_{\mathbf{anthr}}$. In fact, the presence of ruthenium dictates a stiffness of the whole structure, especially when concerning metalla-assemblies ($\mathbf{A_1}$-$\mathbf{A_9}$). The geometrical constraints are important in those kinds of structures and the stabilization of a zwitterionic cation is consequently more difficult. In addition, the decreased reactivity of $\mathbf{A}_{\mathbf{anthr}}$ can also be ascribed to the lower electron density on the anthracenyl core after the coordination of the ruthenium atoms to the pyridyl units. The same phenomenon was also recently

observed by Stang, in collaboration with Fudickar and Linker, on organoplatinum(II) metallacycles [20a]. In addition, we could see that not all the curves were linear: this is the case for a majority of molecules derived from **L_3**, **L_7** (vinylpyridinyl linkers) and **L_4** (ethynylpyridinyl linkers). Therefore, they are not following the same kinetics, thus suggesting that the cycloaddition might proceed *via* other mechanisms. This can explain the special behavior of **A_6** and the particular enhancement of reactivity of **A_7** compared to the unreactive **L_4**.

Table 2: Determination for **L_{anthr}** and **A_{anthr}** of k' and their corresponding absolute second order rate constant (k) values, based on literature data for DPA [44].

	k' (s^{-1})	**k ($x10^6$ $M^{-1}\cdot s^{-1}$)**
DPA	6.14×10^{-4}	4.20
L_1	1.50×10^{-4}	1.02
L_2	1.91×10^{-4}	1.31
L_4	8.20×10^{-6}	0.06
L_5	4.47×10^{-5}	0.31
L_6	1.35×10^{-4}	0.92
A_1	1.53×10^{-5}	0.10
A_2	4.07×10^{-5}	0.28
A_3	8.52×10^{-4}	0.58
A_4	5.15×10^{-6}	0.04
A_5	5.65×10^{-5}	0.39
A_{10}	3.37×10^{-5}	0.23
A_{11}	4.78×10^{-5}	0.33
A_{13}	6.37×10^{-5}	0.44
A_{14}	1.08×10^{-4}	0.74
A_{15}	4.78×10^{-5}	0.58

3.3. Cell culture and photocytotoxicity of A_{anthr}

The toxicity and photocytotoxicity of **L_{anthr}** and **A_{anthr}** were determined by performing MTT assays (MTT = 3-(4,5-dimethylthiazol-2-yl)-2,5-diphenyltetrazoliumbromide) on DU145 prostatic cancer cells. Dark- and phototoxicity were tested, with and without TPP. The dose-response results are presented in Table 3 and in Fig. S6. In addition,

from the MTT assays, IC_{50} values were calculated and the phototoxic index (PI) was estimated (Table 3). PI is the ratio of the IC_{50} in the dark to the IC_{50} upon light irradiation: the higher is PI, the higher is the phototoxicity index. However, the results of MTT assays are not showing a real phototoxicity of the tested anthracenyl derivatives $\mathbf{L_{anthr}}$ and $\mathbf{A_{anthr}}$ on DU145 prostatic cancer cells at those concentrations, except for $\mathbf{A_8}$ and $\mathbf{A_{10}}$, for which the curves showed a clear difference between the dark and under light conditions. Nevertheless, these experiments put in light two special cases. First, the particular behavior of $\mathbf{A_6}$ to act as a photosensitizer and secondly, the addition of TPP significantly improved the toxicity of $\mathbf{A_7}$: its IC_{50} concentration is decreased by a factor of around 4.5 when TPP is added to the medium.

Table 3: IC_{50} (in nM) and phototoxic index values of TPP, $\mathbf{L_1}$-$\mathbf{L_4}$ and $\mathbf{A_1}$-$\mathbf{A_{15}}$. Values calculated with the data of MTT assays on DU145 prostatic cancer cells. “n.d”, for values not determined; “-“, for conditions non tested. Data obtained with the software GraphPad.

	Product alone		**Product with TPP**		**Phototoxic index**	
	non irradiated	*irradiated*	*non irradiated*	*irradiated*	*without TPP*	*with TPP*
TPP	-	-	1993 ± 333	853.5 ± 84	-	2.3
$\mathbf{L_1}$	630.4 ± 96	525.9 ± 38	450.4 ± 48	387.2 ± 37	1.2	1.2
$\mathbf{L_2}$	705.9 ± 61	643.5 ± 56	370.5 ± 40	420.0 ± 47	1.1	0.9
$\mathbf{L_3}$	544.0 ± 33	563.3 ± 56	396.2 ± 36	382.5 ±33	1.0	1.0
$\mathbf{L_4}$	681.9 ± 44	586.3 ± 41	336.3 ± 43	254.7 ± 44	1.2	1.3
$\mathbf{A_1}$	n.d.	n.d.	n.d.	n.d.	n.d.	n.d.
$\mathbf{A_2}$	n.d.	n.d.	n.d.	929.9 ± 99	n.d.	n.d.
$\mathbf{A_3}$	878.7 ± 29	800.9 ± 65	851.2 ± 43	722.0 ± 25	1.1	1.2
$\mathbf{A_4}$	1028.0 ± 145	n.d.	n.d.	902.3 ± 33	n.d.	n.d.
$\mathbf{A_5}$	750.4 ± 16	690.8 ± 22	679.5 ± 16	521.9 ± 13	1,1	1.3
$\mathbf{A_6}$	n.d.	n.d.	946.5 ± 25	936.8 ± 24	n.d.	1.0
$\mathbf{A_7}$	2106.0 ± 1769	1325.0 ± 261	466.4 ± 47	402.5 ± 54	1.6	1.2
$\mathbf{A_8}$	766.3 ± 96	784.2 ± 97	557.3 ± 58	330.2 ± 31	1.0	1.7
$\mathbf{A_9}$	152.5 ± 46	138.5 ± 49	97.6 ± 21	83.4 ± 21	1.1	1.2

A_{10}	547.3 ± 37	345.4 ± 50	336.7 ± 23	233.5 ± 28	1.6	1.4
A_{11}	556.0 ± 45	504.0 ± 31	480.8 ± 30	468.5 ± 48	1.1	1.0
A_{13}	452.0 ± 56	414.5 ± 77	431.3 ± 57	411.2 ± 65	1.1	1.0
A_{14}	343.0 ± 28	266.2 ± 25	305.3 ± 35	263.5 ± 30	1.3	1.2
A_{15}	207.7 ± 15	231.5 ± 27	305.3 ± 35	263.5 ± 30	0.9	1.2

4. Conclusions

We have presented the synthesis and the characterization of 15 arene ruthenium(II) complexes **A_1**-**A_{15}**. They were subjected to several studies to determine their ability to capture oxygen. For the majority of them, the formation of the endoperoxide derivatives were clearly confirmed by spectroscopic techniques and especially by mass spectrometry. One goal of this work was to determine whether the introduction of arene ruthenium(II) and the formation of complexes will increase the reactivity of **A_1**-**A_{15}** towards oxygen. It appears that the complexation of anthracenyl derivatives decreases the formation of endoperoxide species. However, despite this behavior, two metalla-assemblies have showed interesting properties, **A_6** can perform both, oxygen trapping and photo-activation, while **A_7** was more phototoxic on DU145 prostatic cancer cells in the presence of TPP, suggesting a possible synergetic effect when a photosensitizer is added.

Acknowledgments
The authors acknowledge financial support from the University of Neuchâtel (Switzerland) and the implication of the different teams for the analytical part of this work. D.L.S. is thankful to the European Union through the NOAH project (H2020-MSCA-ITN project Ref. 765297) for funding.

References

[1] Fior R. (2019) In: Fior R., Zilhão, R. (ed) Cancer – when Cells Break the Rules and Hijack Their Own Planet. Molecular and Cell Biology of Cancer. Springer Nature Switzerland AG, Cham, Switzerland.

[2] Sutcliffe S. B. (2014) In: Stewart B. W., Wild C. P. (ed) National cancer control plans. World Cancer Report 2014. The international Agency for Research on Cancer: Lyon, France.

[3] Luo W., Wang Y. (2019) In: Gilkes D. M. (ed) Hypoxia Mediates Tumor Malignancy and Therapy Resistance. Hypoxia and Cancer Metastasis, Springer Nature Switzerland: Cham, Switzerland.

[4] Al Tameemi W., Dale T. P., Al-Jumaily R. M. K., Forsyth N. R. (2019) Hypoxia-Modified Cancer Cell Metabolism. Front. Cell Dev. Biol. 7:1-15. https://doi.org/10.3389/fcell.2019.00004

[5] Mckeown S. R. (2014 Defining normoxia, physoxia and hypoxia in tumour-implications for treatment response. Br. J. Radiol. 87:1-12. https://doi.org/10.1259/bjr.20130676

[6] López-Lázaro M. (2008) The warburg effect: why and how do cancer cells activate glycolysis in the presence of oxygen? Anti-Cancer Agents Med. Chem. 8:305-312. https://doi.org/10.2174/187152008783961932

[7] Schlie K., Spowart J. E., Hughson L. R., Townsend K. N., Lum J. J. (2011) When cells suffocate: autophagy in cancer and immune cells under low oxygen. Int. J. Cell

Biol. 2011:1-13. https://doi.org/10.1155/2011/470597

[8] Semenza G. L., Wang G. L. (1992) A Nuclear Factor Induced by Hypoxia via De Novo Protein Synthesis Binds to the Human Erythropoietin Gene Enhancer at a Site Required for Transcriptional Activation. Mol. Cell Biol. 12:5447-5454. https://doi.org/0.1128/mcb.12.12.5447

[9] Muz B., de la Puente P., Azab F., Azab A. K. (2015 The role of hypoxia in cancer progression, angiogenesis, metastasis, and resistance to therapy. Hypoxia 3:83-92. https://doi.org/10.2147/HP.S93413

[10] Rohwer N., Cramer T. (2011) Hypoxia-mediated drug resistance: Novel insight on the functional interaction of HIFs and cell death pathways. Drug Resist. Updates 14:191-201. https://doi.org/10.1016/j.drup.2011.03.001

[11] Weidemann A., Johnson R. S. (2008) Biology of HIF-1α. Cell Death Differ. 15:621-627. https://doi.org/10.1038/cdd.2008.12

[12] Cooper G. M., Hausman R. E. (2007 In: Cooper G. M., Hausman R. E. (ed) The Cell, A Molecular Approach, 4th edn. The American Society for Microbiology, Washington, USA.

[13] Miller M. E. (2018) In: Campbell A. M. (ed) Treatment and Therapy. Cancer. Momentum Press, New York, USA.

[14] Melford J. (2017) In: Melford J. (ed) A guide to Cancer. Origins and Revelations. CRC Press: Boca Raton, USA.

[15] Grzybowski A., Sak J., Pawlikowski J. (2016) A brief report on the history of phototherapy. Clin. Dermatol. 34:532-537. https://doi.org/10.1016/j.clindermatol.2016.05.002

[16] Agostinis P., Berg K., Cengel K.A., Foster T.H., Girotti A.W., Gollnick S.O., Hahn S.M., Hamblin M.R., Juzeniene A., Kessel D., et al. (2011) Photodynamic therapy of

cancer: An update. CA Cancer J. Clin. 61:250–281. https://doi.org/10.3322/caac.20114

[17] Foote C. S. (1991) Definition of type I and type II photosensitized oxidation. Photochem. Photobiol. 54:659. https://doi.org/10.1111/j.1751-1097.1991.tb02071.x

[18] Debele T.A., Peng S., Tsai H.C. (2015) Drug carrier for photodynamic cancer therapy. Int. J. Mol. Sci. 16:22094–22136. https://doi.org/10.3390/ijms160922094

[19] Callaghan S., Senge M. O. (2018) The good, the bad, and the ugly – controlling singlet oxygen through design of photosensitizers and delivery systems for photodynamic therapy. Photochem. Photobiol. Sci. 17:1490-1514 https://doi.org/10.1039/c8pp00008e

[20] (a) He Y.-Q., Fudickar W., Tang J.-H., Wang H., Li X., Han J., Wang Z., Liu M., Zhong Y.-W., Linker T., Stang P. J. (2020) Capture and Release of Singlet Oxygen in Coordination-Driven Self-Assembled Organoplatinum(II) Metallacyles. J. Am. Chem. Soc. 142:2601–2608. https://doi.org/10.1021/jacs.9b12693 (b) Qin Y., Chen L.-J., Dong F., Yin G.-Q., Li X., Tian Y., Yang H.-B. (2019) Light-Controlled Generation of Singlet Oxygen within a Discrete Dual-Stage Metallacyle for Cancer Therapy. J. Am. Chem. Soc. 141:8943-8950. https://doi.org/10.1021/jacs.9b02726 (c) Sun W., Zeng X., Wu S. (2018) Photoresponsive ruthenium-containing polymers: potential polymeric metallodrugs for anticancer phototherapy. Dalton Trans. 47:283-286. https://doi.org/10.1039/C7DT03390G (d) Rohrabaugh Jr. T. N., Collins K. A., Xue C., White J. K., Kodanko J. J., Turro C. (2018) New Ru(II) complex for dual photochemotherapy: release of cathepsin K inhibitor and $^1O_2$ production. Dalton Trans. 47:11851-11858. https://doi.org/10.1039/C8DT00876K (e) Sun W., Wen Y, Thiramanas R., Chen M., Han J., Gong N., Wagner M., Jiang S., Meijer M. S., Bonnet S., Butt H.-J., Mailänder V., Liang X.-J., Wu S. (2018) Red-Light Controlled Release

of Drug-Ru Complex Conjugates from Metallopolymer Micelles for Phototherapy in Hypoxic Tumor Environments. Adv. Funct. Matter. 28:1804227. https://doi.org/10.1002/adfm.201804227 (f) Frei A., Rubbiani R., Tubafard S., Blacque O., Anstaett P., Felgenträger A., Maisch T., Spiccia L., Gasser G. (2014) Synthesis, Characterization, and Biological Evaluation of New Ru(II) Polypyridyl Photosensitizers for Photodynamic Therapy. J. Med. Chem. 57:7280-7292. https://doi.org/10.1021/jm500566f (g) Davia K., King D., Hong Y., Swavey S. (2008) A porphyrin−ruthenium photosensitizer as a potential photodynamic therapy agent. Inorg. Chem. Commun. 11:584−586. https://doi.org/0.1021/ic8015589 (h) Gianferrara T., Bergamo A., Bratsos I., Milani B., Spagnul C., Sava G., Alessio E. (2010) Ruthenium−porphyrin conjugates with cytotoxic and phototoxic antitumor activity. J. Med. Chem. 53:4678−4690. https://doi.org/10.1021/jm1002588 (i) Pernot M., Bastogne T., Barry N. P. E., Therrien B., Koellensperger G., Hann S., Reshetov V., Barberi-Heyob M. (2012) Systems biology approach for in vivo photodynamic therapy optimization of ruthenium−porphyrin compounds. J. Photochem. Photobiol., B. 117: 80−89. https://doi.org/10.1016/j.jphotobiol.2012.08.012

[21] Schmitt F., Freudenreich J., Barry N. P. E., Juillerat-Jeanneret L., Süss-Fink G., Therrien B. (2012) Organometallic Cages as Vehicles for Intracellular Release of Photosensitizers. Journal of the American Chemical Society 134:754-757. https://doi.org/10.1021/ja207784t

[22] (a) Matsumoto M., Yamada M., Watanabe N. (2005) Reversible 1,4-cycloaddition of a singlet oxygen to N-substituted 2-pyridones: 1,4- endoperoxide as a versatile chemical sourcer of singlet oxygen. Chem.Commun. 2005:483–485. https://doi.org/10.1039/B414845B (b) Wiegand C., Herdtweck E., Bach T. (2012) Enantioselectivity in visible light-induced, singlet oxygen [2+4] cycloaddition reactions

(type II photooxygenations) of 2-pyridones. Chem. Commun. 48:10195–10197. https://doi.org/10.1039/C2CC35621J (c) Benz S., Nötzli S., Siegel J. S., Eberli D., Jessen H. J. (2013) Controlled Oxygen Release from Pyridone Endoperoxides Promotes Cell Survival under Anoxic Conditions. J. Med. Chem. 56:10171–10182 https://doi.org/10.1021/jm4016137 (d) Turan I. S., Yildiz D., Turksoy A., Gunaydin G., Akkaya E. U. (2016) A Bifunctional Photosensitizer for Enhanced Fractional Photodynamic Therapy: Singlet Oxygen Generation in the Presence and Absence of Light. Angew. Chem. Int. Ed. 55:2875-2878. https://doi.org/10.1002/ange.201511345 (e) Xiao W. Y., Wang P., Ou C. J., Huang X. Y., Tang Y. Y., Wu M. Y., Si W. L., Shao J. J., Huang W., Dong X. C. (2018) 2-Pyridone-Functionalized Aza-BODIPY Photosensitizer for Imaging-Guided Sustainable Phototherapy. Biomaterials 183:1-9. https://doi.org/10.1016/j.biomaterials.2018.08.034

[23] (a) [1] Naphthalene endoperoxides as generators of singlet oxygen in biological media. Pierlot C., Aubry J.-M., Briviba K., Sies H., Mascio P. D. (2000) Methods Enzymol. 319:3–20. https://doi.org/10.1016/S0076-6879(00)19003-2 (e) Liu K., Lalancette R. A., Jäkle F. (2019) Tuning the Structure and Electronic Properties of B-N Fused Dipyridylanthracene and Implications on the Self-Sensitized Reactivity with Singlet Oxygen. J. Am. Chem. Soc. 141:7453-7462. https://doi.org/10.1021/jacs.9b01958 (f) Martins S., Farinha J. P. S., Baleizão C., Berberan-Santos M. N. (2014) Controlled release of singlet oxygen using diphenylanthracene functionalized polymer nanoparticules. Chem. Commun. 50:3317-3320. https://doi.org/10.1039/C3CC48293F

[24] (a) Klaper M., Linker T. (2013) Evidence for an oxygen anthracene sandwich complex. Angew. Chem. Int. Ed. 52:11896–11899. https://doi.org/10.1002/anie.201304768 (b) Klaper M., Linker T. (2015) New Singlet

Oxygen Donors Based on Naphthalenes: Synthesis, Physical Chemical Data, and Improved Stability. Chem. - Eur. J. 21:8569-8577. https://doi.org/10.1002/chem.201500146 (c) Fudickar W., Linker T. (2018) Release of Singlet Oxygen from Aromatic Endoperoxides by Chemial Triggers. Angew. Chem. Int. Ed. 57:12971-12975. https://doi.org/10.1002/anie.201806881 (d) Fudickar W., Linker T. (2018) Release of Singlet Oxygen from Organic Peroxides under Mild Conditions. ChemPhoChem. 2:548-558. https://doi.org/10.1002/cptc.201700235

[25] (a) Moureu C., Dufraisse C., Dean P. M. (1926) Un peroxyde organique dissociable : le peroxyde de rubrène. Comptes Rendus Acad. Sci. 182:1584-1587 (b) Dufraisse C., Velluz L. (1942) L'union labile de l'oxygène au carbone. Influences des méthoxyles et de leurs positions sur l'état de labilité de l'oxygène dans les photooxydes mésodiphénylanthracéniques : un peroxide spontanlment dissociable à froid. Bull. Soc. Chim. Fr. 171-184.

[26] (a) Foote C. S., Wexler S. (1964) Olefin oxidations with excited singlet oxygen. J. Am. Chem. Soc. 86:3879-3880. (b) Wasserman H. H., Scheffer J. R. (1967) Singlet oxygen reactions from photoperoxides. J. Am. Chem. Soc. 89:3073-3075.

[27] (a) Arbuzov Y. A. (1965) The Diels-Alder reaction with molecular oxygen dienophile. Russ. Chem. Rev. 34:558. (b) Clennan, E. L. (1991) Synthethic and mechanistic aspects of 1,3-diene photooxidation. Tetrahedron, 47:1343-1382. https://doi.org/10.1016/S0040-4020(01)86413-9

[28] (a) Reddy A. R., Bendikov M. (2006) Diels–Alder reaction of acenes with singlet and triplet oxygen – theoretical study of two-state reactivity. Chem. Commun. 2006:1179-1181. https://doi.org/10.1039/B513597D (b) Aubry J.-M., Pierlot C., Rigaudy J., Schmidt R. (2003) Reversible binding of oxygen to aromatic compounds. Acc. Chem. Res. 36:668-675. https://doi.org/10.1021/ar010086g

[29] (a) Zhu J., Zou J., Zhang J., Sun Y., Dong X., Zhang Q. (2019) Anthracene functionalized BODIPY derivative with singlet oxygen storage ability for photothermal and continuous photodynamic synergistic therapy. J. Mater. Chem. B. 7:3303-3309. https://doi.org/10.1039/C9TB00180H (b) Callaghan S., Filatov M. A., Savoie H., Boyle R. W., Senge M. O. (2019) In vitro cytotoxicity of a library of BODIPY-anthracene and -pyrene dyads for application in photodynamic therapy. Photochem. Photobiol. Sci. 18:495-504. https://doi.org/10.1039/C8PP00402A (c) Su W., Dong S., Chen X., Xiao J.-A., Peng B., Li P. (2019) Novel half-sandwich rhodium(III) and iridium(III) photosensitizers for dual chemo- and photodynamic therapy. Photodiagn. Photodyn. Ther. 26:448-454. https://doi.org/10.1016/j.pdpdt.2019.04.028 (d) Das D., Banaspati A., Das N., Bora B., Raza M. K., Goswami T. K. (2019) Visible light-induced cytotoxicity studies on Co(II) complexes having an anthracene-based curcuminoid ligand. Dalton Trans. 2019:12933-12942. https://doi.org/10.1039/C9DT01576K

[30] Fudickar W., Linker T. (2017) Synthesis of Pyridylanthracenes and Their Reversible Reaction with Singlet Oxygen to Endoperoxides. J. Org. Chem. 82:9258-9262. https://doi.org/10.1021/acs.joc.7b01765

[31] Yan H., Süss-Fink G., Neels A., Stoeckli-Evans H. (1997) Mono-, di- and tetra-nuclear p-cymene ruthenium complexes containing oxalato ligands. J. Chem. Soc. Dalton Trans. 1997:4345–4350. https://doi.org/10.1039/A704658H

[32] Therrien B., Süss-Fink G., Govindaswamy P., Renfrew A.K., Dyson P.J. (2008) The “complex-in-a-complex” cations $[(acac)_2M\subset Ru_6(p\text{-}iPrC_6H_4Me)_6(tpt)_2(dhbq)_3]^{6+}$: A trojan horse for cancer cells. Angew. Chem. Int. Ed. Engl. 47:3773–3776. https://doi.org/10.1002/anie.200800186

[33] Barry N.P.E., Therrien B. (2009) Host–Guest Chemistry in the Hexanuclear (Arene)ruthenium Metalla-Prismatic Cage $[Ru_6(p\text{-}cymene)_6(tpt)_2(dhnq)_3]^{6+}$. Eur. J.

Inorg. Chem. 2009:4695–4700. https://doi.org/10.1002/ejic.200900649

[34] Allardyce C. S., Dyson P. J., Ellis D. J., Heath S. L. (2001) [Ru(η^6-p-cymene)Cl_2(pta)] (pta = 1,3,5-triaza-7-phosphatricyclo- [3.3.1.1]decane): a water soluble compound that exhibits pH dependent DNA binding providing selectivity for diseased cells. Chem. Commun. 2001:1396-1397. https://doi.org/10.1039/B104021A

[35] Bennett M. A., Huang T.- N., Matheson T. W., Smith A. K. (1982) (η^6-Hexamethylbenzene)Ruthenium Complexes. Inorg. Chem., 21:74-78: https://doi.org/10.1002/9780470132524.ch16

[36] Fudickar W., Linker T. (2017) Synthesis of Pyridylanthracenes and Their Reversible Reaction with Singlet Oxygen to Endoperoxides. J. Org. Chem. 82:9258-9262. https://doi.org/10.1021/acs.joc.7b01765

[37] Chien W.-L., Yang C.-M., Chen T.-L., Li S.-T., Hong J.-L. (2013) Enhanced emission of a pyridine-based luminogen by hydrogen-bonding to organic and polymeric phenols. RSC Adv. 3:6930-6938. https://doi.org/10.1039/C3RA22217A

[38] Shih K.-Y, Lin Y.-C., Hsiao T.-S-, Deng S.-L., Kuo S.-W., Hong J.-L. (2014) Amorphous and crystalline blends from polytyrosine and pyridine-functionalized anthracene: hydrogen-bond interactions, conformations, intramolecular charge transfer and aggregation-induced emission. Polym. Chem. 5:5765-5774. https://doi.org/10.1039/C4PY00706A

[39] Ciesielski A., Piot L., Samorì P., Jouaiti A., Hosseini M.W. (2009) Molecular tectonics at the solid/liquid interface: Controlling of 1D coordination networks on graphite surfaces. Adv. Mater. 21:1131–1136. https://doi.org/10.1002/adma.200801776

[40] Gaschard M., Nehzat F., Cheminel T., Therrien B. (2018) Arene Ruthenium Metalla-Assemblies with Anthracene Moieties for PDT Applications. Inorganics 6:97. https://doi.org/10.1002/adma.200801776

[41] Mattsson J., Govindaswamy P., Renfrew A. K., Dyson P. J., Štěpnička P., Süss-Fink G., Therrien B. (2009) Synthesis, Molecular Structure, and Anticancer Activity of Cationic Arene Ruthenium Metallarectangles. Organometallics 28:4350-4357. https://doi.org/10.1021/om900359j

[42] Barry N. P. E., Zava O., Dyson P. J., Therrien B. (2011) Excellent Correlation between Drug Release and Portal Size in Metalla-Cage Drug-Delivery Systems. Chem. Eur. J. 17:9669-9677. https://doi.org/10.1002/chem.201003530

[43] Fudickar W., Linker T. (2012) Why Triple Bonds Protect Acenes from Oxidation and Decomposition. J. Am. Chem. Soc. 134:15071-15082. https://doi.org/10.1021/ja306056x

[44] Wilkinson F. (1995) Rate Constants for the Decay and Reactions of the Lowest Electronically Excited Singlet State of Molecular Oxygen in Solution. An Expanded and Revised Compilation. J. of Physical and Chemical Reference Data 24:663-1021. https://doi.org/10.1063/1.555965

SUPPORTING INFORMATION

A Strategy to Trap Oxygen and to Kill Cancer Cells by Photodynamic Therapy.

Marie Gaschard,[a] Daniel L. Stares,[b] Manuel A. Gallardo-Villagrán,[ac] David Yannick Leger,[c] Bertrand Liagre,[c] Christoph A. Schalley[b] and Bruno Therrien[a*]

[a] Institute of Chemistry, University of Neuchâtel, Avenue de Bellevaux 51, 2000 Neuchâtel, Switzerland.

[b] Institute of Chemistry and Biochemistry of Freie Universität Berlin, Arnimallee 20, 14195 Berlin, Germany.

[c] Département de Biochimie et Biologie Moléculaire, Laboratoire PEIRENE, Faculté de Pharmacie, 2 rue du Docteur Marcland, 87025 Limoges, France.

*corresponding author: bruno.therrien@unine.ch

1. Synthesis and characterization of L_1-L_7

1.1. General procedure for 9,10-bis(pyridyl)anthracene (L_1 and L_2) [1]

9,10-Dibromoanthracene (1.00 g, 2.98 mmol), 4-pyridylboronic acid (914 mg, 7.44 mmol, for **L_1**) or 3-pyridylboronic acid (914 mg, 7.44 mmol, for **L_2**), potassium carbonate (4.11 g, 20 mmol) and tetrakis(triphenylphosphine) palladium(0) (344 mg, 0.29 mmol) were dissolved in DMF (80 mL) and H_2O (10 mL). Three cycles of freeze pumping were realized. After stirring for 12 h at 105 °C, the solvents were removed under vacuum. The residue was dissolved in $CHCl_3$ and then extracted with the same solvent. The organic layer was twice washed with H_2O. Hydrochloric acid (1 M) was slowly added until the aqueous pH reached 1and became yellow. The organic phase was discarded. Then, potassium hydroxide (1 M) was slowly added, until the aqueous pH reached 8. The product was isolated by another extraction using $CHCl_3$. The evaporation of the solvent, after drying the organic phase over dried $MgSO_4$, gave the desired product. When needed, a column chromatography (silica gel; EtOAc) was realized for further purification.

9,10-bis(4-pyridyl)anthracene (L_1) pale-yellow solid (633 mg; 64%). ^{1}H-NMR ($CDCl_3$, 400 MHz). δ 8.89 (dd, *J* = 4.4 Hz and *J* = 1.6 Hz , 4H), 7.62 (dd, *J* = 6.8 Hz and *J* = 3.2 Hz, 4H), 7.45 (dd, *J* = 4.4 Hz and *J* = 1.6 Hz , 4H), 7.40 (dd, *J* = 6.8 Hz and *J* = 3.2 Hz, 4H).^{13}C{^{1}H}-NMR ($CDCl_3$, 100 MHz). δ 150.3 (4C), 147.5 (2C), 134.9 (2C), 129.2 (4C), 126.6 (4C), 126.5 (4C), 126.1 (4C).

9,10-bis(3-pyridyl)anthracene (L_2) pale-yellow solid (742 mg; 75%). ^{1}H-NMR ($CDCl_3$, 400 MHz). δ 8.84 (dd, *J* = 4.8 Hz and *J* = 1.6 Hz, 2H), 8.75 (dd, *J* = 4.8 Hz and *J* = 2.4

Hz, 2H), 7.84 (m, 2H), 7.64 (dd, *J* = 6.8 Hz and *J* = 3.6 Hz, 4H), 7.59 (m, 2H), 7.40 (dd, *J* = 8.0 Hz and *J* = 3.2 Hz, 4H). $^{13}C\{^{1}H\}$-NMR ($CDCl_3$, 100 MHz). δ 152.0 (1C), 151.9 (1C), 149.3 (2C), 139.0 (1C), 138.9 (1C), 134.8 (2C), 133.9 (2C), 130.3 (2C), 126,6 (4C), 126.0 (4C), 123.6 (1C), 123.6 (1C).

1.2. Procedure for 9,10-bis((pyridin-4-yl)vinyl)anthracene (L_3) [2,3]

9,10-Dibromoanthracene (1.00 g, 2.98 mmol), 4-vinylpyridine (625 mg, 5.94 mmol), palladium(II)acetate (67 mg, 0.30 mmol), triphenylphosphine (156 mg, 0.60 mmol) and triethylamine (600 mg, 5.93 mmol) were dissolved in dried DMF (20 mL). Nitrogen was bubbled through the solution in a Schlenk flask for 20 min. After stirring 24 h at 115 °C, the solution was poured into H_2O. The product was extracted several times with CH_2Cl_2 and the combined organic phases were washed with brine, dried over $MgSO_4$ and concentrated by rotary evaporator. The crude product was purified by column chromatography (silica gel; hexane/EtOAc = 4/1). The pure product was obtained as a yellow solid (229 mg; 27%). ^{1}H-NMR ($CDCl_3$, 400 MHz). δ 8.70 (m, 4H), 8.33 (dd, *J* = 6.8 Hz and *J* = 3.2 Hz, 4H), 8.17 (d, *J* = 16.4 Hz, 2H), 7.56 (m, 4H), 7.52 (dd, *J* = 6.8 Hz and *J* = 3.2 Hz, 2H), 6.91 (d, *J* = 16.4 Hz, 2H). $^{13}C\{^{1}H\}$-NMR ($CDCl_3$, 100 MHz). δ 150.6 (4C), 144.5 (2C), 135.4 (2C), 132.3 (2C), 130.2 (2C), 129.6 (4C), 126.3 (4C), 126.0 (4C), 121.2 (4C).

1.3. Procedure for 9,10-bis(3,3'-ethynylpyridyl)anthracene (L_4) [4,5]

In a Schlenk flask, a mixture of 9,10-dibromoanthracene (400 mg, 1.19 mmol) and 3-ethynylpyridine (270 mg, 2.62 mmol) was dissolved in a solution of toluene/Et_3N (1/1, 25 mL) and kept under a nitrogen atmosphere for 20 min. Then, a mixture of palladium(II)acetate (5 mg, 0.024 mmol), copper(I)iodide (6 mg, 0.030 mmol) and triphenylphosphine (17 mg, 0.065 mmol) was added with the other reactants. The reaction mixture was stirred at reflux for 24 h. Then, the solvent was removed under

vacuum. The residue was dissolved in H_2O and stirred for 2 h at room temperature, to eliminate the triethylammonium salt. The solid was filtered off and dried under vacuum. Recrystallization was done in toluene and the product was obtained as orange needles, which were dried under vacuum (285 mg, 63%).^{1}H-NMR ($CDCl_3$, 400 MHz): δ 9.02 (s, 2H), 8.66 (m, 6H), 8.06 (d, *J* = 7.6 Hz, 2H), 7.69 (m, 4H), 7.42 (m, 2H). ^{13}C{^{1}H}-NMR ($CDCl_3$, 100 MHz): δ 152.4 (2C), 149.2 (2C), 138.6 (2C), 132.3 (4C), 127.4 (4C), 127.3 (4C), 123.4 (2C), 120.7 (2C), 118.4 (2C), 99.12 (2C), 89.77 (2C).

1.4. General procedure for 9-(pyridyl)anthracene (L_5 and L_6) [1]

9-Bromoanthracene (1.00 g, 3.89 mmol), 4-pyridylboronic acid (526 mg, 4.28 mmol, for **L_5**) or 3-pyridylboronic acid (526 mg, 4.28 mmol, for **L_6**), potassium carbonate (5.39 g, 39 mmol) and tetrakis(triphenylphosphine) palladium(0) (451 mg, 0.39 mmol) were dissolved in THF (40 mL) and H_2O (20 mL). Three cycles of freeze pumping were realized. After stirring 48 h at 110 °C, the solvents were removed under vacuum. The residue was extracted with EtOAc several times. The organic layer was twice washed with brine and dried over $MgSO_4$. Then, the solvent was removed by rotary evaporation. The crude product was recrystallized from hot acetone to yield a pure white powder.

9-(4-pyridyl)anthracene (L_5) (436 mg, 44%). ^{1}H-NMR ($CDCl_3$, 400 MHz). δ 8.85 (d, *J* = 5.2 Hz, 2H), 8.55 (s, 1H), 8.06 (d, *J* = 8.4 Hz, 2H), 7.57 (d, *J* = 8.8 Hz, 2H), 7.49 (t, *J* = 7.4 Hz, 2H), 7.39 (m, 4H). ^{13}C{^{1}H}-NMR ($CDCl_3$, 100 MHz). δ 150.1 (2C), 147.6 (1C), 137.7 (1C), 131.4 (2C), 129.6 (2C), 128.7 (2C), 127.7 (1C), 126.6 (2C), 126.2 (2C), 126.0 (2C), 125.5 (2C).

9-(3-pyridyl)anthracene (L_6) (626 mg, 63%). ^{1}H-NMR ($CDCl_3$, 400 MHz). δ 8.81 (d, *J* = 4.8 Hz, 1H), 8.71 (s, 1H), 8.56 (s, 1H), 8.08 (d, *J* = 4.2 Hz, 2H), 7.79 (dd, *J* = 7.6 Hz, 1H), 7.59 (d, *J* = 4.4 Hz, 2H), 7.55 (t, *J* = 6.8 Hz, 1H), 7.49 (t, *J* = 7.4 Hz, 2H), 7.39 (m,

2H). $^{13}C\{^{1}H\}$-NMR ($CDCl_3$, 100 MHz). δ 150.1 (2C), 147.6 (1C), 137.7 (1C), 131.4 (2C), 129.6 (2C), 128.7 (2C), 127.7 (1C), 126.6 (2C), 126.2 (2C), 126.0 (2C), 125.5 (2C). IR (cm^{-1}): 3050 (w; C-H aromatic), 1403 and 1027 (m; C=C aromatic), 741 (s, C-H aromatic). ESI-MS (+): m/z = 256.1 $[M+H]^+$. UV−vis [1.0 x 10^{-5} M, CH_2Cl_2; λ_{max}, nm (ε, $M^{-1}.m^{-1}$)]: 253 (1.1 × 10^5), 333 (0.8 × 10^4), 349 (1.6 × 10^4), 367 (2.3 × 10^4), 387 (2.3 × 10^4), 399 (2.9 × 10^4). Anal. calc. for $C_{19}H_{13}N$ (255.33): C 89.38, H 5.13, N 5.49; Found: C 89.21, H 5.15, N 5.34.

1.5. Procedure for 9-((pyridin-4-yl)vinyl)anthracene (L_7) [2,3]

9-Bromoanthracene (500 mg, 1.94 mmol), 4-vinylpyridine (322 mg, 3.06 mmol), palladium(II)acetate (46 mg, 0.19 mmol), triphenylphosphine (102 mg, 0.39 mmol) were dissolved in a mixture of dried DMF (10 mL) and Et_3N (0,5 mL). Nitrogen was bubbled into the solution for 20 min. After stirring 24 h at 115 °C, H_2O (10 mL) was added. The product was extracted several times with CH_2Cl_2 and the combined organic phases were washed with brine, dried over $MgSO_4$ and concentrated by rotary evaporator. The crude product was purified by column chromatography (silica gel; hexane/EtOAc = 4/1 to 1/1). The pure product was obtained as a yellow solid (398 mg; 73%). ^{1}H-NMR ($CDCl_3$, 400 MHz). δ 8.68 (d, *J* = 6 Hz, 2H), 8.45 (s, 1H), 8.28 (s, 2H), 8.15 (d, *J* = 16.4 Hz, 1H), 8.06 (m, 2H), 7.53 (d, *J* = 6 Hz, 2H), 7.50 (dd, *J* = 6.4 Hz and *J* = 3.4 Hz, 4H), 6.92 (d, *J* = 16.4 Hz, 1H). $^{13}C\{^{1}H\}$-NMR ($CDCl_3$, 100 MHz). δ 150.6 (2C), 144.5 (2C), 135.1 (1C), 131.6 (2C), 131.4 (2C), 130.0 (1C), 129.8 (1C), 129.0 (2C), 127.4 (1C), 126.1 (2C), 125.7 (2C), 125.5 (2C), 121.1 (2C).

2. X-ray crystallography

Crystals were mounted on a Stoe Image Plate Diffraction system equipped with a Φ circle goniometer, using Mo Kα graphite monochromated radiation (λ = 0.71073 Å) with

Φ range 0-200°. The structures were solved by direct methods using the program *SHELXS-97* [6], while the refinement and all further calculations were carried out using *SHELXL-97*. The H-atoms were included in calculated positions and treated as riding atoms using *SHELXL-97* default parameters. The non-H atoms were refined anisotropically using weighted full-matrix least-square on F^2. Crystallographic details are summarized in Table S1 and in Fig. 4 of the article, drawn with *ORTEP-32* [7].

CCDC-2081638 (**L$_6$**) contains the supplementary crystallographic data for this paper, which can be obtained free of charge at www.ccdc.cam.ac.uk/conts/retrieving.html (or from the Cambridge Crystallographic Data Center, 12, Union Road, Cambridge CB2 1EZ, UK; fax: (internat.) +44-1223/336-033; E-mail: deposit@ccdc.cam.ac.uk).

Table S1. Crystallographic data and structure refinement parameters for **L$_6$**.

	L$_6$
Chemical formula	$C_{19}H_{13}N$
Formula weight	255.33
Crystal system	monoclinic
Space group	*P* 2_1
Crystal size (mm^3)	0.20 × 0.18 × 0.17
Crystal color and shape	colorless block
a (Å)	9.2682(11)
b (Å)	13.8896(17)
c (Å)	11.0542(12)
α (°)	90
β (°)	113.744(8)
γ (°)	90
cell volume ($Å^3$)	1302.57
T (K)	293(2)
Z	4
Scan range (°)	2.40 < θ < 26.21
ρ_{calcd} (g cm^{-3})	1.302
μ (mm^{-1})	0.076
Unique reflections	2611
Reflections used [$I > 2\sigma(I)$]	1959
R_{int}	0.0244
Final *R* indices [$I > 2\sigma(I)$][a]	0.0608, wR_2 0.1040
R indices (all data)[b]	0.0396, wR_2 0.0912

GOF[c]	1.074
Max, min $\Delta\rho/e$ (Å^{-3})	1.138, -0.124

[a] $R_1 = \Sigma||F_o| - |F_c||/\Sigma|F_o|$. [b] $wR_2 = \{\Sigma[w(F_o^2 - F_c^2)^2]/\Sigma[w(F_o^2)^2]\}^{1/2}$. [c] GOF = $\{\Sigma[w(F_o^2 - F_c^2)^2]/(n - p)\}^{1/2}$, where n is the number of reflections and p is the total number of parameters refined.

3. Mass spectrometry data for A_1-A_{15}

Table S2: *m/z* values from ESI-MS spectra for A_1-A_{15}.

Assembly	**Formula**	**ESI-MS peaks expected**	**ESI-MS peaks found**
A_1	$[M\text{-}4(CF_3SO_3^-)]^{4+}$: $[M\text{-}3(CF_3SO_3^-)]^{3+}$: $[M\text{-}2(CF_3SO_3^-)]^{2+}$:	470.5744 677.0833 1090.6013	Not received/ measured
A_2	$[M\text{-}4(CF_3SO_3^-)]^{4+}$: $[M\text{-}3(CF_3SO_3^-)]^{3+}$: $[M\text{-}2(CF_3SO_3^-)]^{2+}$:	470.5744 677.0833 1090.6013	470.5762 677.0856 1090.6073
A_3	$[M\text{-}4(CF_3SO_3^-)]^{4+}$: $[M\text{-}3(CF_3SO_3^-)]^{3+}$: $[M\text{-}2(CF_3SO_3^-)]^{2+}$:	1053.09028	Not found, only fragments
A_4	$[M\text{-}4(CF_3SO_3^-)]^{4+}$: $[M\text{-}3(CF_3SO_3^-)]^{3+}$:	470.5743 677.0833	470.5762 677.0860
A_5	$[M\text{-}4(CF_3SO_3^-)]^{4+}$: $[M\text{-}3(CF_3SO_3^-)]^{3+}$: $[M\text{-}2(CF_3SO_3^-)]^{2+}$:		Not found, only fragments
A_6	$[M\text{-}4(CF_3SO_3^-)]^{4+}$:	496.5901	496.5914
A_7	$[M\text{-}2(CF_3SO_3^-)]^{2+}$ $[M\text{-}(CF_3SO_3^-)]^{+}$: $[M\text{-}2\mathbf{L_4}\text{-}2(CF_3SO_3^-)]^{4+}$:		Not found, only fragments
A_8	$[M\text{-}2(CF_3SO_3^-)]^{2+}$: $[M\text{-}(CF_3SO_3^-)]^{+}$: $[M\text{-}2\mathbf{L_4}\text{-}2(CF_3SO_3^-)]^{4+}$:		Not found, only fragments
A_9	$[M\text{-}2(CF_3SO_3^-)]^{2+}$: $[M\text{-}2\mathbf{L_4}\text{-}2(CF_3SO_3^-)]^{4+}$:		Not found, only fragments
A_{10}	$[M\text{-}2(CF_3SO_3^-)]^{2+}$: $[M\text{-}(CF_3SO_3^-)]^{+}$:	594.1256 1337.2036	594.1252 1337.2053
A_{11}	$[M\text{-}2(CF_3SO_3^-)]^{2+}$: $[M\text{-}(CF_3SO_3^-)]^{+}$:	594.1256 1337.2036	594.1252 1337.2053
A_{12}	$[M\text{-}(CF_3SO_3^-)]^{+}$:	620.1456	620.1422
A_{13}	$[M\text{-}2(CF_3SO_3^-)]^{2+}$: $[M\text{-}(CF_3SO_3^-)]^{+}$:	618.1256 1384.2041	618.1249 1384.2079
A_{14}	$[M\text{-}(CF_3SO_3^-)]^{+}$:	683.1644	683.1612
A_{15}	$[M\text{-}(CF_3SO_3^-)]^{+}$:	683.1644	683.1669

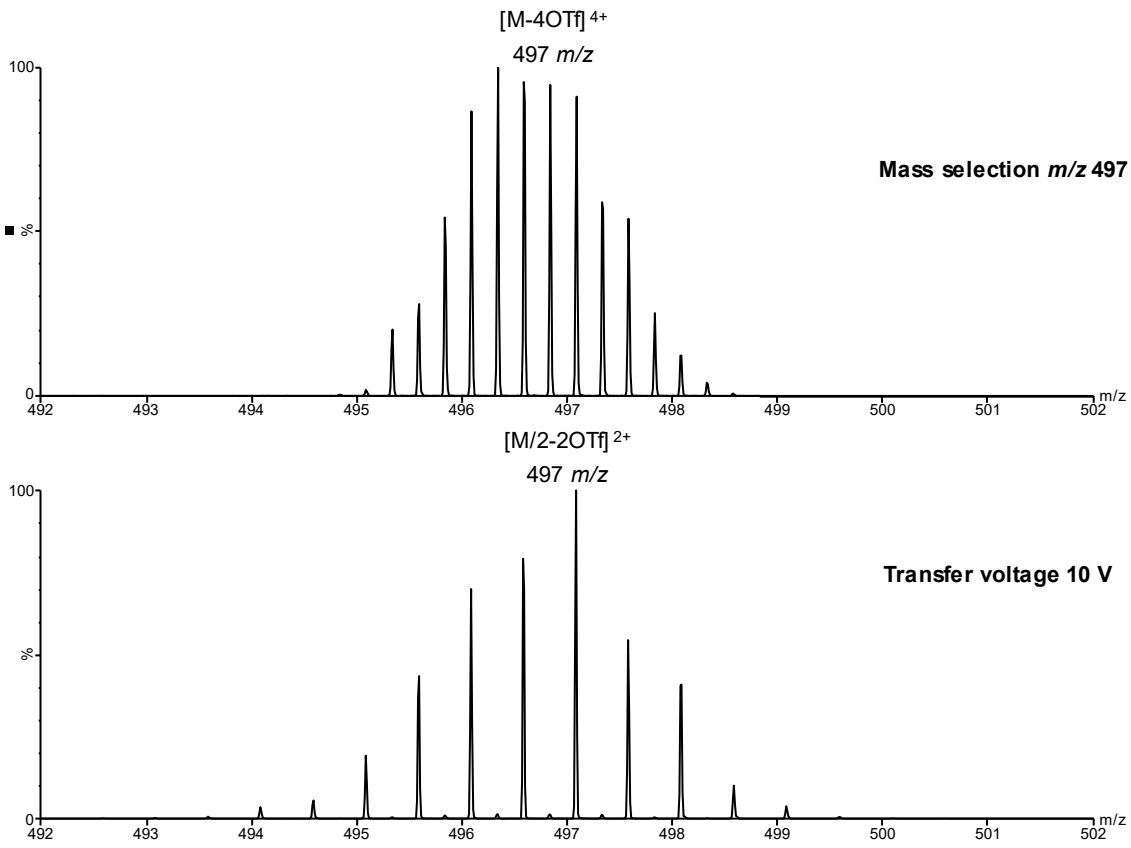

Fig. S1. CID measurements of the mass selected $[M\text{-}4OTf]^{4+}$ of **A6**. This fragmentation produces the +2 half which can overlap with the $[M\text{-}4OTf]^{4+}$ ion.

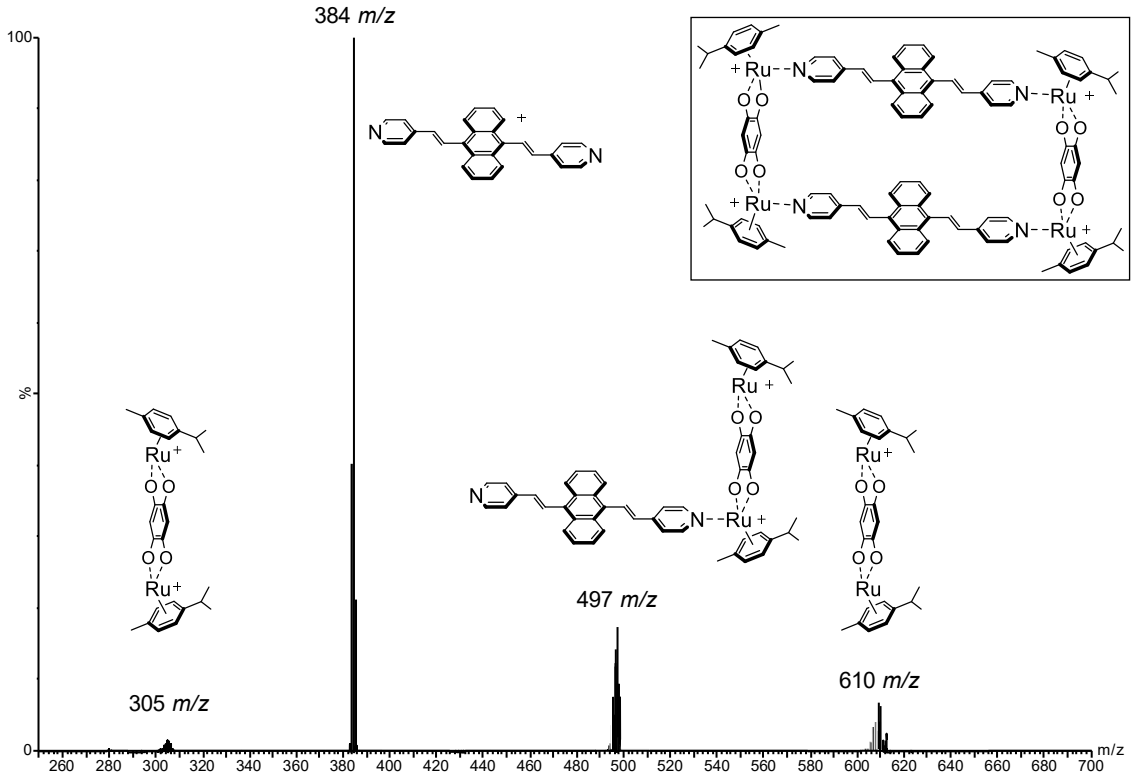

Fig. S2. Full spectrum of CID measurements of the mass selected $[M\text{-}4OTf]^{4+}$ of **A6** at a transfer voltage of 15 V. This fragmentation produces the +1 and +2 sides as well as the +1 ligand in a charge transfer process.

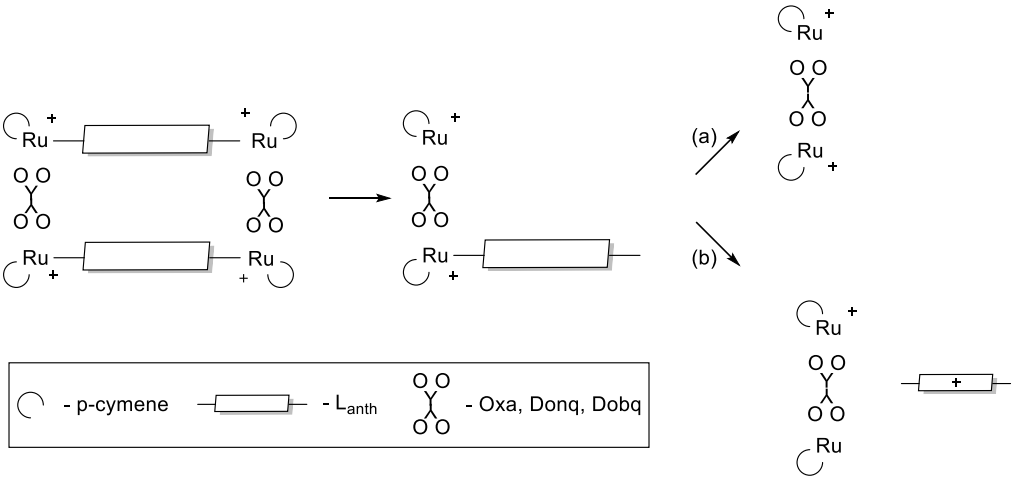

Scheme S1. Fragmentation pathway of the Ruthenium arene cages. The intact cage will split via the Ruthenium nitrogen bond to produce the half cage. This half has two fragmentation pathways either (a) direct cleavage of the $\mathbf{L_{anth}}$ pathway to produce the doubly charged side or via (b) which proceeds via a charge separation to produce the singly charged ligand in addition the singly charged $\mathbf{L_{anth}}$

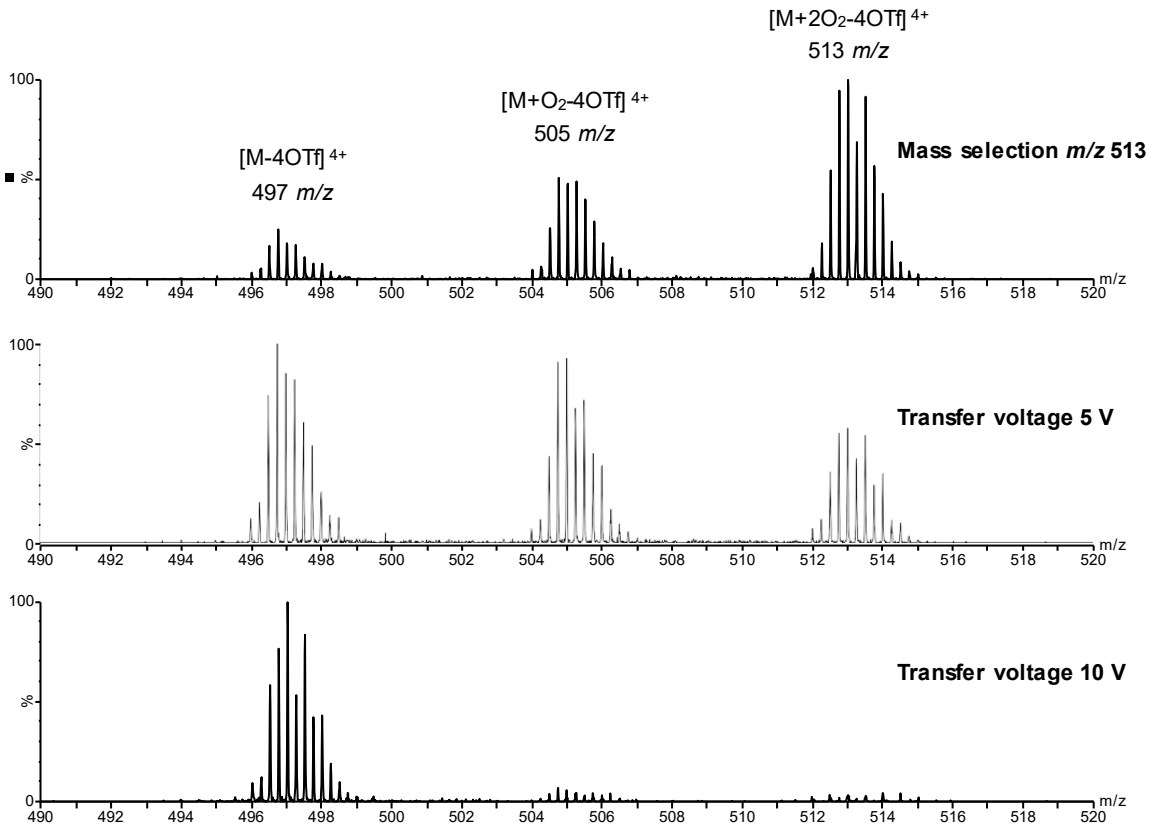

Fig. S3. CID measurements of the mass selected $[M+2O_2\text{-}4OTf]^{4+}$ of **A6**. Oxygen loss occurs at low CID energies before the fragmentation of the assembly.

4. Photooxygenation studies

3.1. ^{1}H NMR experiments

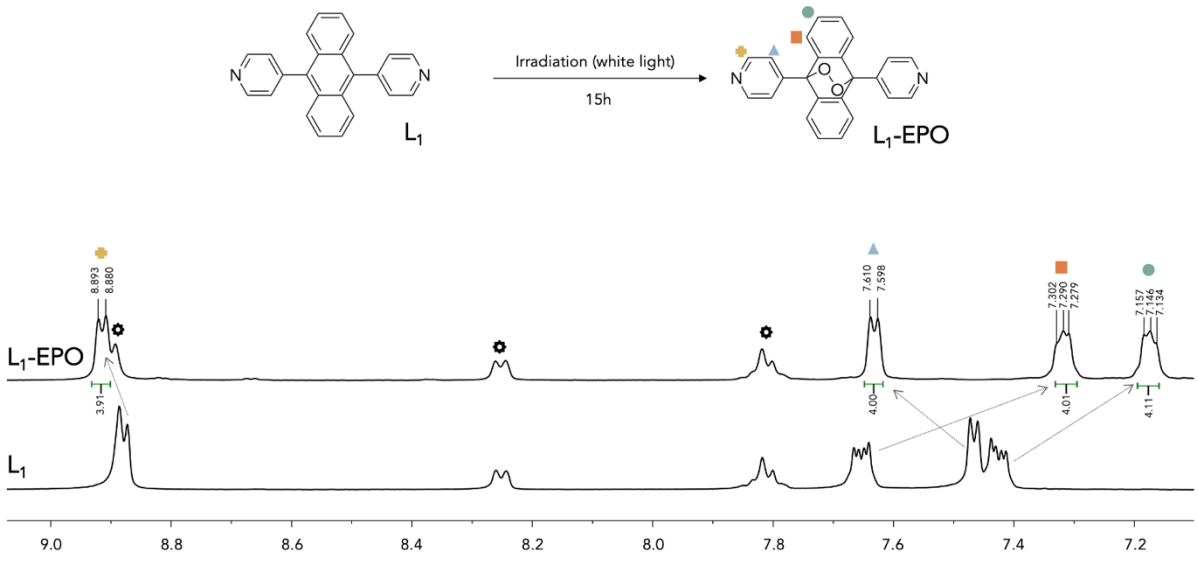

Fig. S1. ^{1}H NMR spectra of $\mathbf{L_1}$ with TPP (⭘), before and after irradiation (1 mM, CD_2Cl_2, 23 °C, 400 MHz). The signal shifts show the formation of $\mathbf{L_1}$**-EPO**.

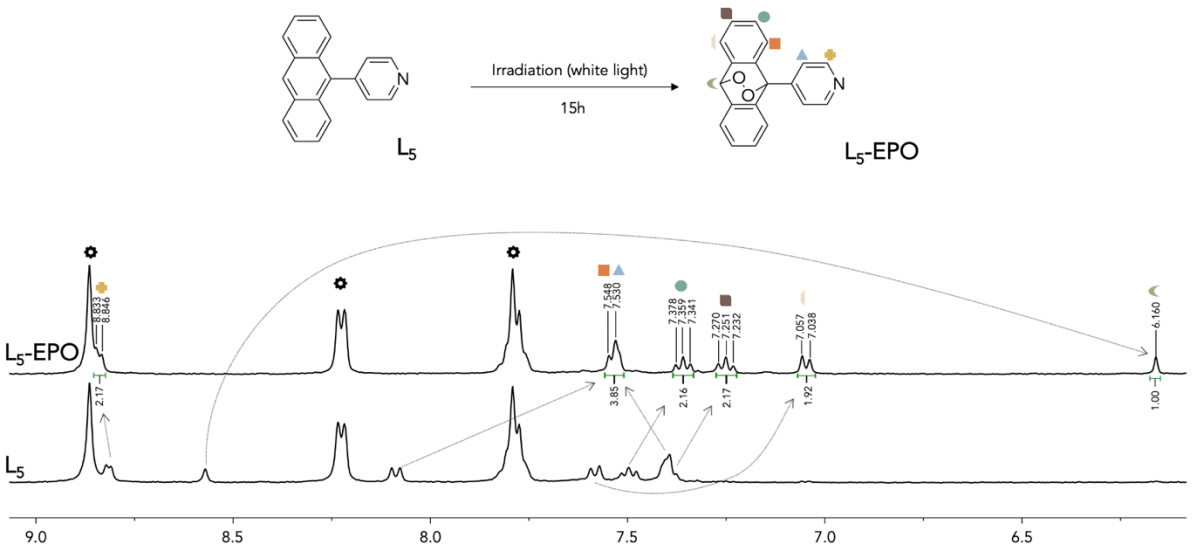

Fig. S2. ^{1}H NMR spectra of **L_5** with TPP (✪), before and after irradiation (1 mM, CD_2Cl_2, 23 °C, 400 MHz). The signal shifts show the formation of **L_5-EPO**.

3.2. UV-Vis experiments

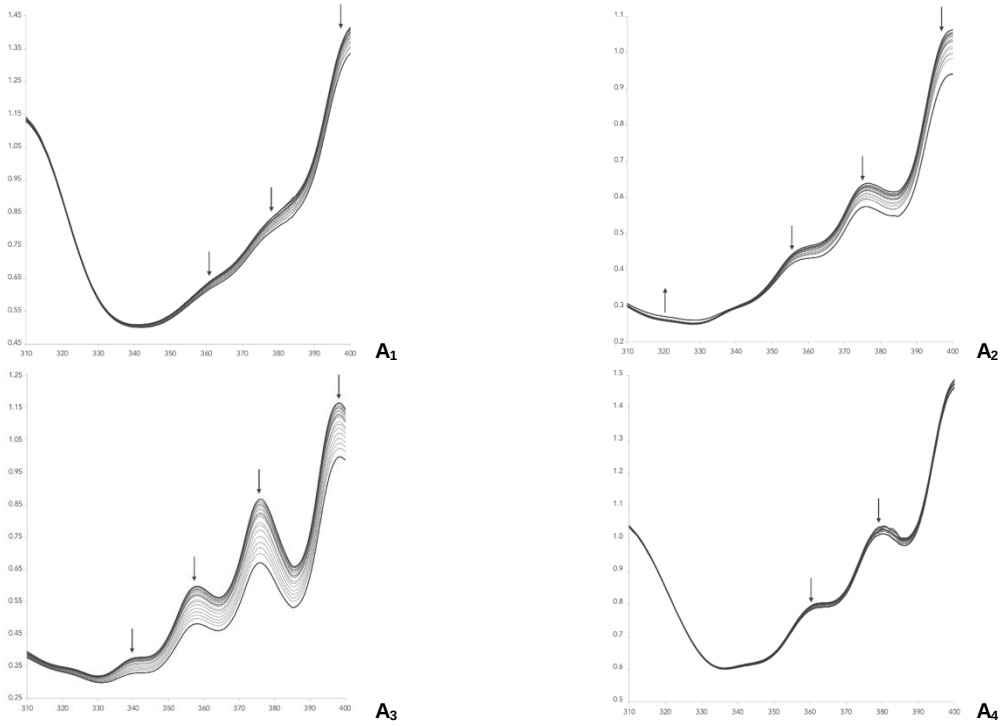

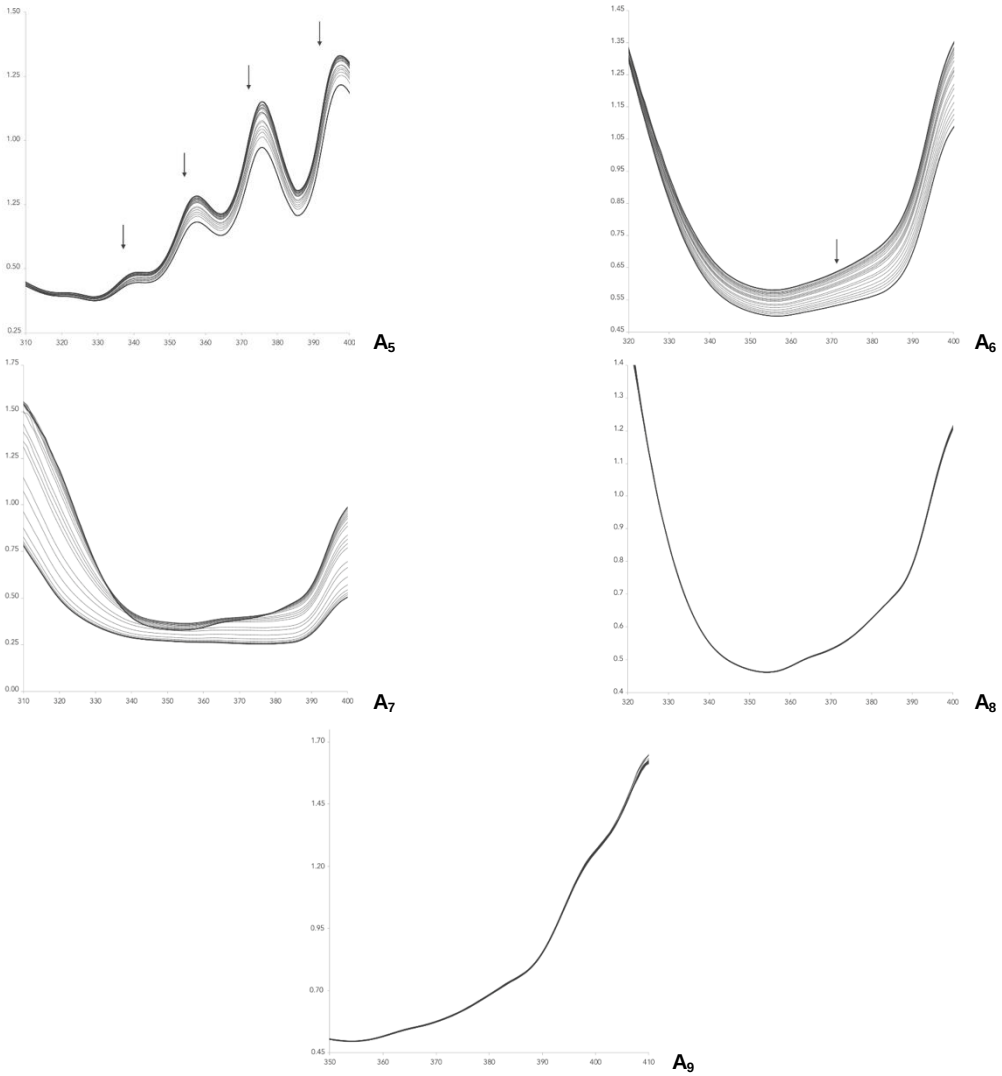

Fig. S3. UV-VIS spectra of **A_1-A_9** (5.0 x 10^{-5} M in CH_3CN/CH_2Cl_2) during irradiation (white light; t = 0 to 60 min; with TPP).

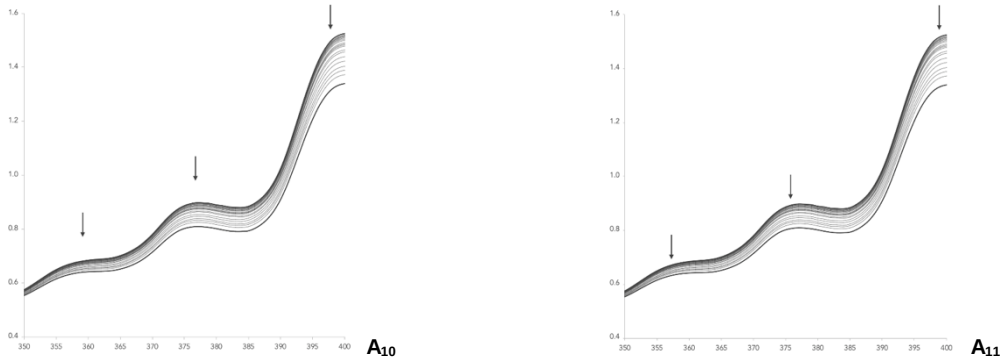

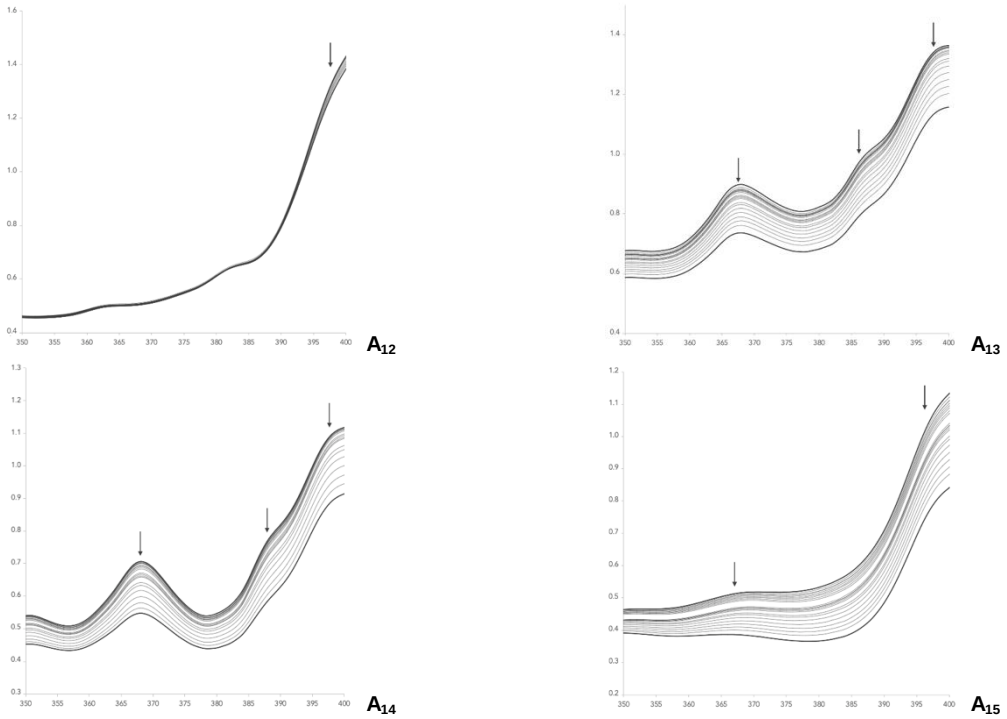

Fig. S4. UV-VIS spectra of **A_{10}-A_{15}** (5.0×10^{-5} M in CH_3CN/CH_2Cl_2) during irradiation (white light; t = 0 to 60 min; with TPP).

3.3. Kinetics of the photooxygenation

3.3.1. Theoretical details

The reaction of the photooxygenation is described by equation (1). "Anthr" is a general term for the molecule, both **L_{anthr}** or **A_{anthr}**, that reacts with $^1O_2$, to afford "Anthr-EPO"

$$\text{Anthr} + {}^1O_2 \rightarrow \text{Anthr-EPO} \quad (1)$$

$$v = \frac{d[\text{anthr}-\text{EPO}]}{dt} = -\frac{d[\text{anthr}]}{dt} = k \cdot [\text{anthr}] \cdot [{}^1O_2] \quad (2)$$

The rate of this reaction is proportional to the concentration of the two reactants, Anthr and $^1O_2$, as explained in equation (2). So, the photooxygenation of **L_{anthr}** and **A_{anthr}** corresponds to a second-order reaction, but it can be simplified. In fact, the concentration of $^1O_2$ can be assumed to be constant, as it is in excess compared to "Anthr". The reaction becomes then a pseudo-first order reaction. The equation (2) can be simplified by equation (3), and gives by the following equation (4).

$$v = k \cdot [\text{anthr}] \cdot [{}^1O_2] = k' \cdot [\text{anthr}] \qquad \text{where } k = k'[{}^1O_2] \qquad (3)$$

$$v = -\frac{d[\text{anthr}]}{dt} = k' \cdot [\text{anthr}]$$

$$\Leftrightarrow \quad -\frac{d[\text{anthr}]}{[\text{anthr}]} = k' \cdot dt$$

$$\Leftrightarrow \quad -\int_{[\text{anthr}]_0}^{[\text{anthr}]} \frac{d[\text{anthr}]}{[\text{anthr}]} = k' \cdot \int_0^t dt$$

$$\Leftrightarrow \quad \ln\left(\frac{[\text{anthr}]_0}{[\text{anthr}]}\right) = k' \cdot t$$

$$\Leftrightarrow \quad \ln\left(\frac{[\text{anthr}]}{[\text{anthr}]_0}\right) = -k' \cdot t \qquad (4)$$

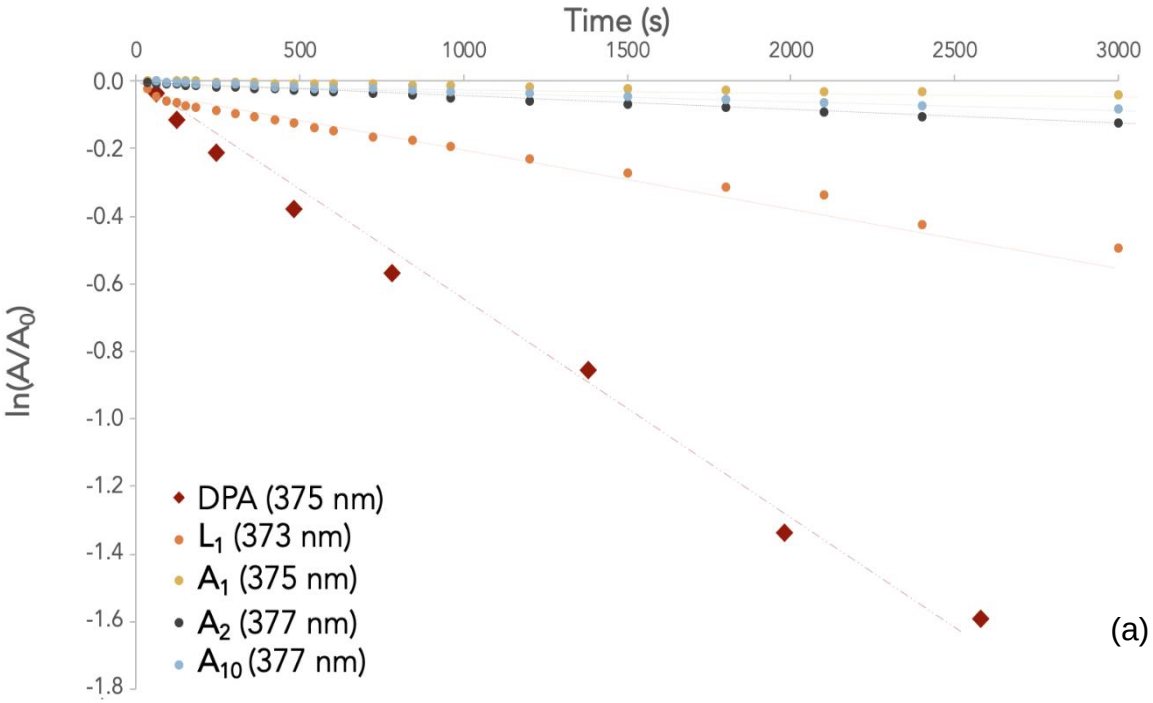
Time (s)
0
500
1000
1500
2000
2500
3000
0.0
-0.2
-0.4
-0.6
-0.8
-1.0
-1.2
-1.4
-1.6
-1.8
ln(A/A0)
DPA (375 nm)
L1 (373 nm)
A1 (375 nm)
A2 (377 nm)
A10 (377 nm)

(a)

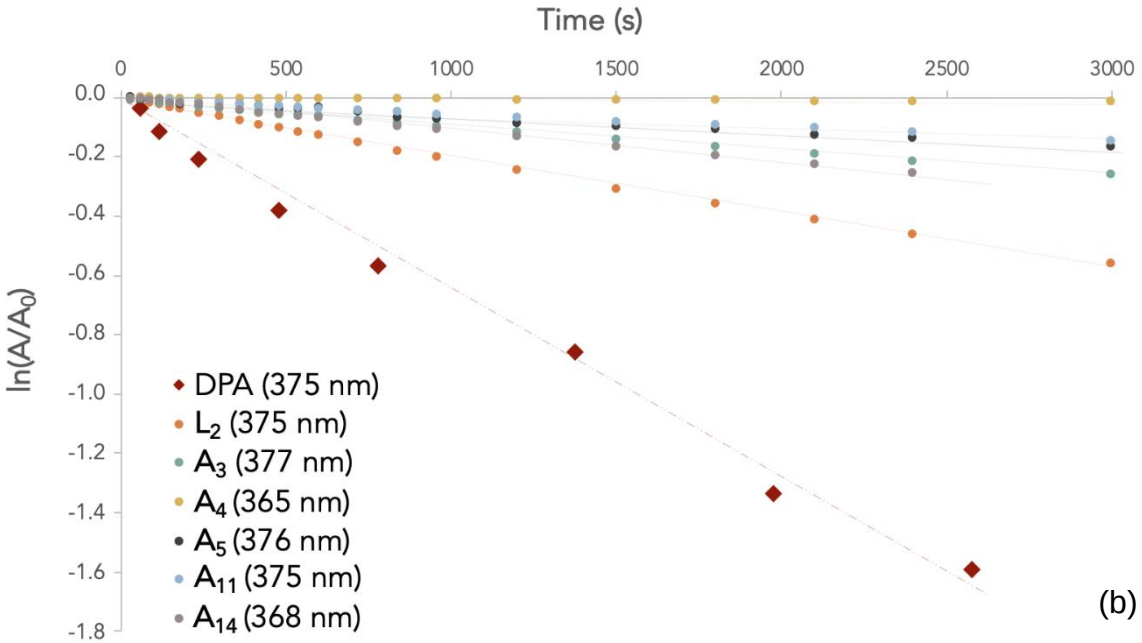
Time (s)
0
500
1000
1500
2000
2500
3000
0.0
-0.2
-0.4
-0.6
-0.8
-1.0
-1.2
-1.4
-1.6
-1.8
ln(A/A0)
DPA (375 nm)
L2 (375 nm)
A3 (377 nm)
A4 (365 nm)
A5 (376 nm)
A11 (375 nm)
A14 (368 nm)

(b)

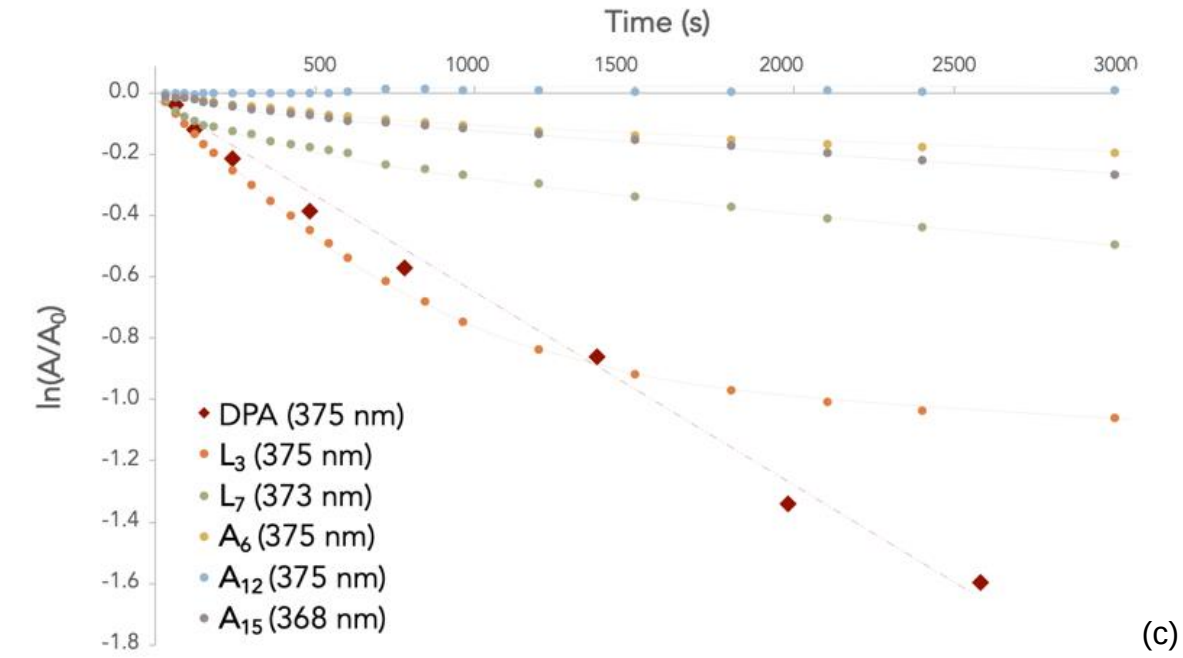

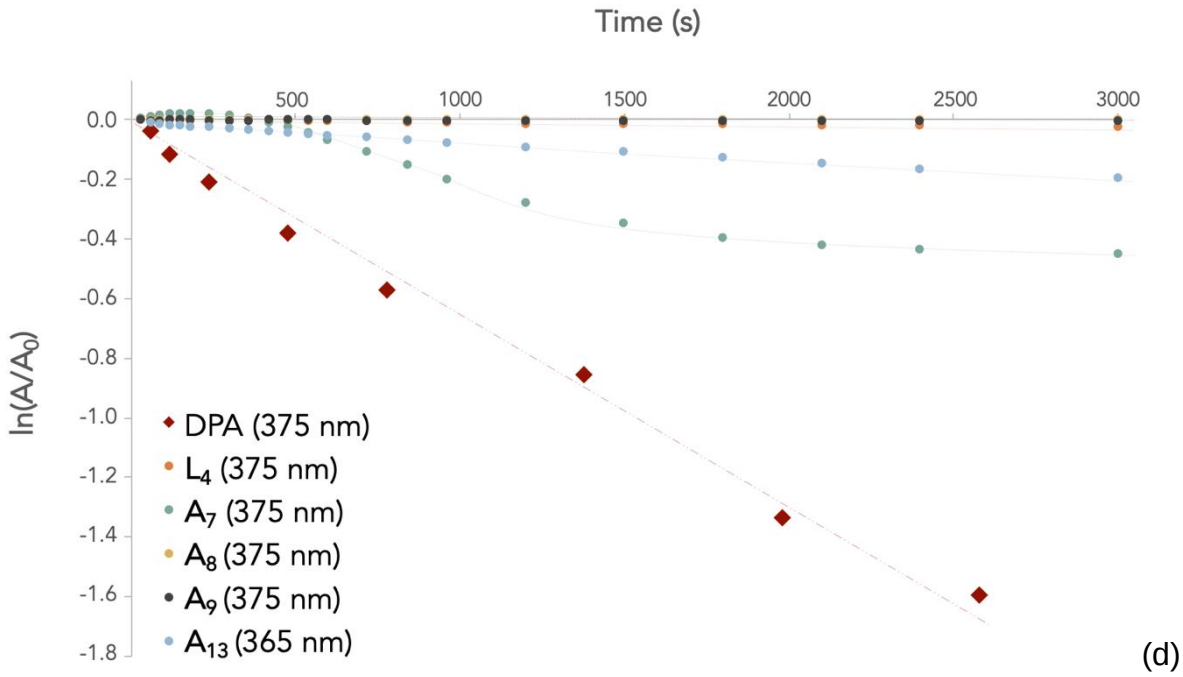

Fig. S5. Semi logarithmic plots of the photooxygenation of: (a) **L_1** derivatives, (b) **L_2** derivatives, (c) **L_3** derivatives and (d) **L_4** derivatives.

5. Phototoxicity on DU143 prostatic cancer cells

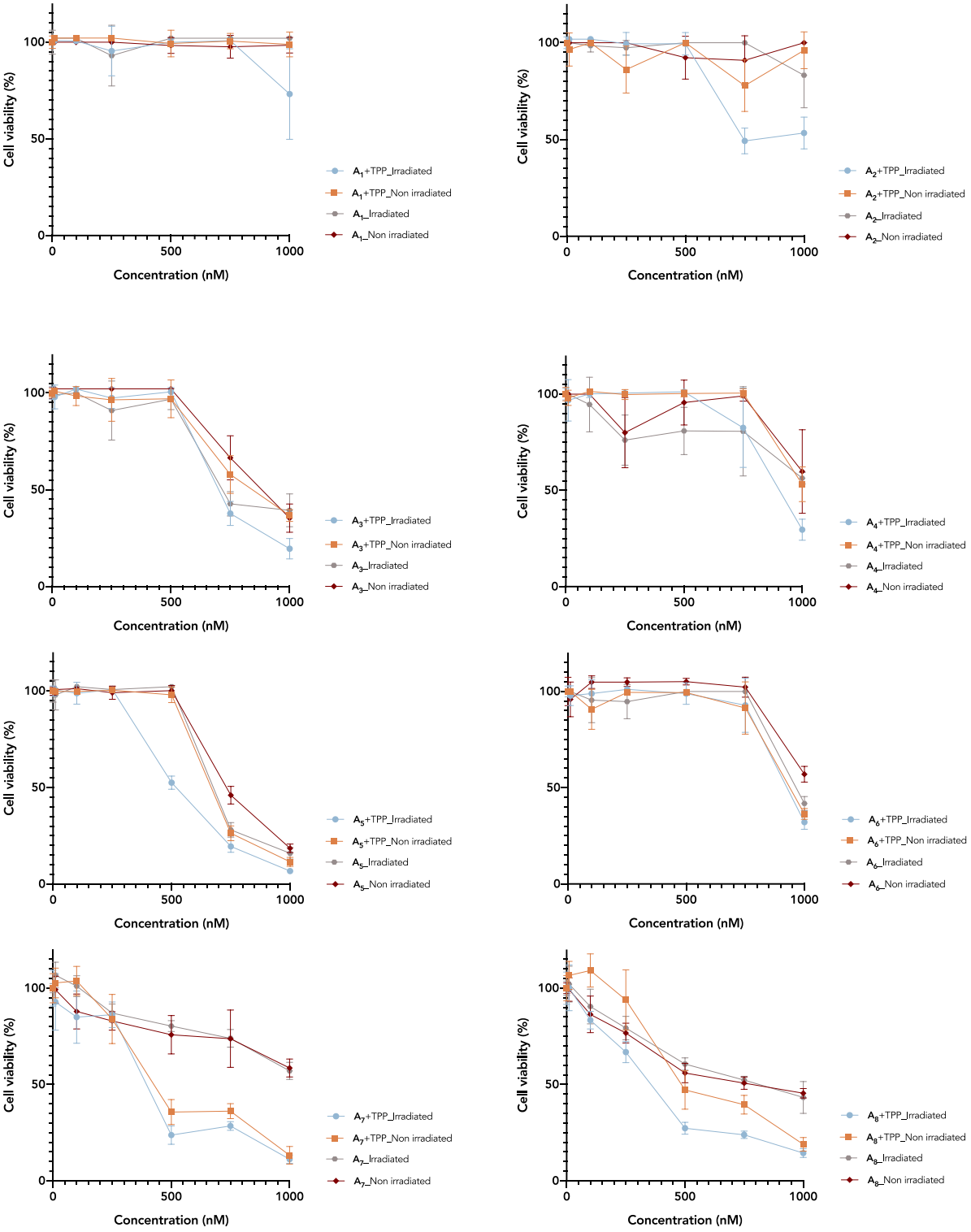

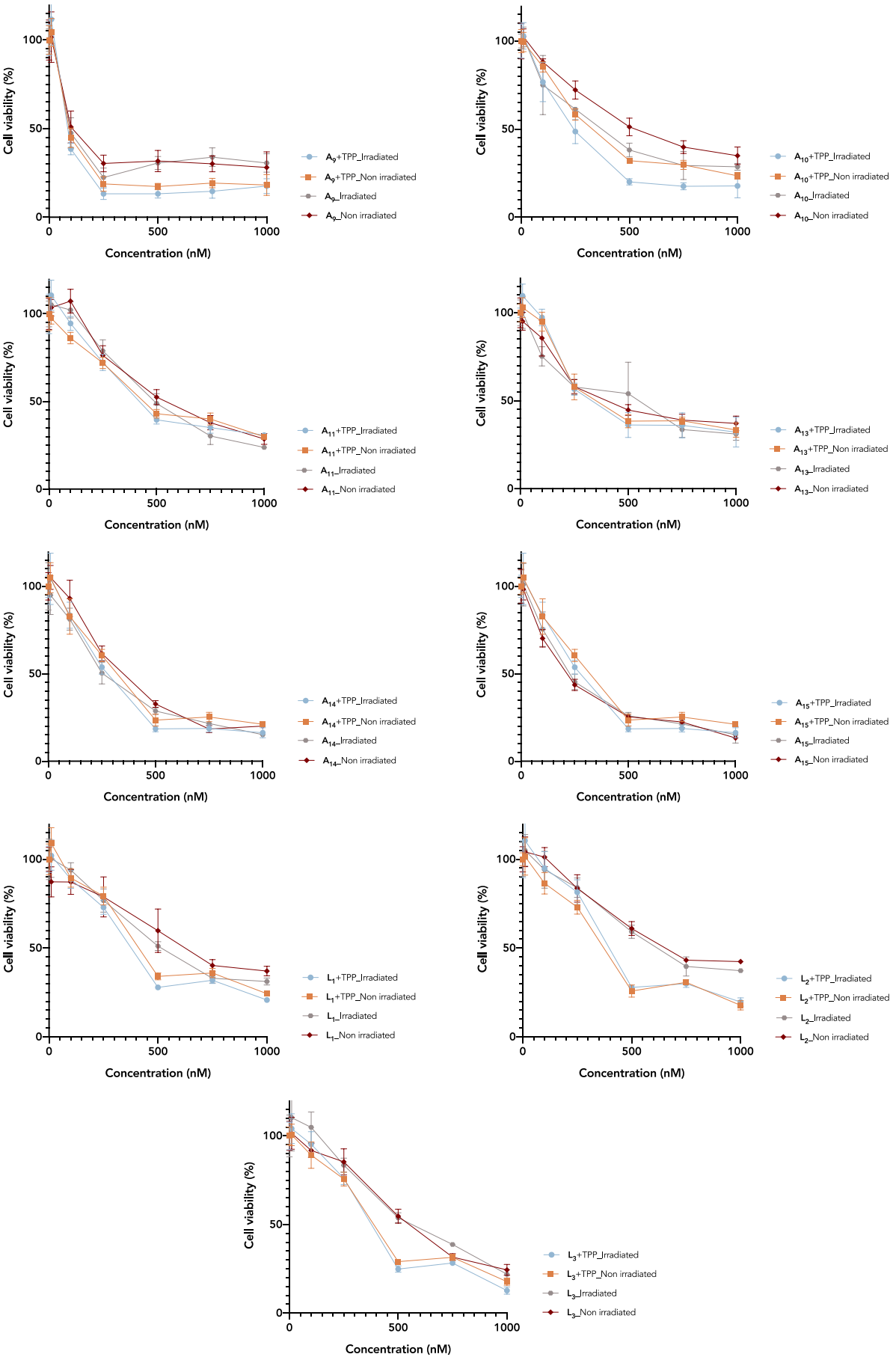
Cell viability (%)
Concentration (nM)
0
50
100
500
1000
A9+TPP_Irradiated
A9+TPP_Non irradiated
A9_Irradiated
A9_Non irradiated
A10+TPP_Irradiated
A10+TPP_Non irradiated
A10_Irradiated
A10_Non irradiated
A11+TPP_Irradiated
A11+TPP_Non irradiated
A11_Irradiated
A11_Non irradiated
A13+TPP_Irradiated
A13+TPP_Non irradiated
A13_Irradiated
A13_Non irradiated
A14+TPP_Irradiated
A14+TPP_Non irradiated
A14_Irradiated
A14_Non irradiated
A15+TPP_Irradiated
A15+TPP_Non irradiated
A15_Irradiated
A15_Non irradiated
L1+TPP_Irradiated
L1+TPP_Non irradiated
L1_Irradiated
L1_Non irradiated
L2+TPP_Irradiated
L2+TPP_Non irradiated
L2_Irradiated
L2_Non irradiated
L3+TPP_Irradiated
L3+TPP_Non irradiated
L3_Irradiated
L3_Non irradiated

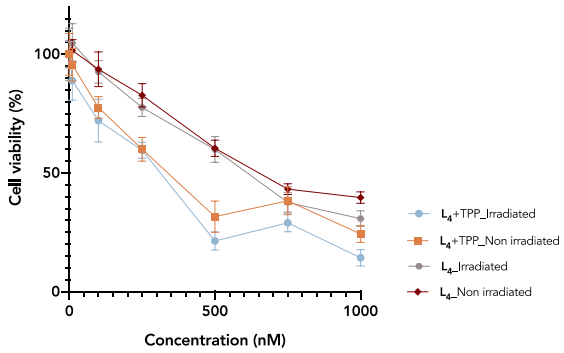

Fig. S6. MTT assays and determination of dark and phototoxicity of $\mathbf{L_{anthr}}$ and $\mathbf{A_{anthr.}}$

6. References

[1] Fudickar W., Linker T. (2017) Synthesis of Pyridylanthracenes and Their Reversible Reaction with Singlet Oxygen to Endoperoxides. J. Org. Chem. 82:9258-9262. https://doi.org/10.1021/acs.joc.7b01765

[2] Chien W.-L., Yang C.-M., Chen T.-L., Li S.-T., Hong J.-L. (2013) Enhanced emission of a pyridine-based luminogen by hydrogen-bonding to organic and polymeric phenols. RSC Adv. 3:6930-6938. https://doi.org/10.1039/C3RA22217A

[3] Shih K.-Y, Lin Y.-C., Hsiao T.-S-, Deng S.-L., Kuo S.-W., Hong J.-L. (2014) Amorphous and crystalline blends from polytyrosine and pyridine-functionalized anthracene: hydrogen-bond interactions, conformations, intramolecular charge transfer and aggregation-induced emission. Polym. Chem. 5:5765-5774. https://doi.org/10.1039/C4PY00706A

[4] Ciesielski A., Piot L., Samorì P., Jouaiti A., Hosseini M.W. (2009) Molecular tectonics at the solid/liquid interface: Controlling of 1D coordination networks on

graphite surfaces. Adv. Mater. 21:1131–1136. https://doi.org/10.1002/adma.200801776

[40] Gaschard M., Nehzat F., Cheminel T., Therrien B. (2018) Arene Ruthenium Metalla-Assemblies with Anthracene Moieties for PDT Applications. Inorganics 6:97. https://doi.org/10.1002/adma.200801776

[6] Sheldrick G. M. (2008) A short history of SHELX. Acta Crystallogr A. 64:112-122. https://doi.org/10.1107/S0108767307043930

[7] Farrugia, L. J. (1997) ORTEP-3 for Windows - a version of ORTEP-III with a Graphical User Interface (GUI). J. Appl. Cryst. 30:565. https://doi.org/10.1107/S0021889897003117